TECHNISCHE
UNIVERSITÄT
WIEN
Vienna University of Technology

LUNDS UNIVERSITET
Lunds Tekniska Högskola

Development of electrical characterization techniques for nanowire based GaN

ANDREAS MODERBACHER, BSc

Solid State Physics
Faculty of Electrical Engineering at Vienna
University of Technology
Faculty of Engineering (LTH) at Lund University
Lund, Sweden 2014
Diploma Thesis 2014:2

Abstract

The title of the thesis is "Development of electrical characterization techniques for nanowire based GaN" and was carried out by Andreas Moderbacher under supervision of Jonas Ohlsson (QuNano AB), Kristian Storm (faculty of engineering at Lund University) and Jürgen Smoliner (Institut for Solid State Electronics at Vienna University of Technology) in 2014.

The aim of this thesis was to develop a process which enables electrical characterization techniques on nanoscale GaN structures to find the density and mobility of charge carriers.

Contacting these structures in a way that allows measurements was a main goal and was achieved successfully. Working independently with clean room facilities after gaining experience with the procedures and equipment needed for the processing was essential therefore. Two-point measurements and four-point measurements were successfully implemented. Following these initial results, preliminary Hall measurements on the nanowire-based GaN were also performed.

Table of Contents

1

Introduction

1.1 Motivation

Gallium nitride attracted a lot of interest for high power electronics due to several reasons, the most important to the semiconductor industry being:

Band gap: GaN is a III/V semiconductor with a wide, direct band gap of 3.4 eV which enables optoelectronic applications, especially for blue and white light-emitting diodes (LED's) as well as high power- and high temperature ($> 700\,^{\circ}\mathrm{C}$) devices. With the increase of temperature, the concentration of minority carriers increases as well, when a certain temperature is reached an extrinsic semiconductor behaves like an intrinsic semiconductor therefore, but for wide band gap materials such as GaN this temperature is much higher than for Ge, Si or GaAs, thus less cooling and heat extraction is needed for GaN devices.[1]

$$E = hf, \qquad \lambda = \frac{c}{f} \tag{1.1}$$

Where
E = band gap (3,4eV),
h = Planck constant,
f = Frequency,
λ = Wavelength and
c = Speed of light.

Its direct wide band gap allows to manufacture light emitting diodes (LEDs) and laser diodes (LDs) emitting light at the shorter wavelengths of the light spectrum, which corresponds to the colors green, blue or violet for instance, without using nonlinear frequency-doubling. Nitride semiconductors are therefore the most promising material for short wavelengths LEDs and LDs. In eq. (1.1) can be seen that a high band gap results in a high frequency since h is a constant, which in turn leads to a low wavelength. III/V nitride semiconductors are important to develop full-color displays. GaN-based blue and green LEDs in combination with GaAs-based red LEDs serve as the basis for large-scale full displays as well as a white light source. By mixing these three colors a compact white light source with a high lifetime can be produced. Furthermore these semiconductor based white light source could save theoretically 80-90% of the power consumption in comparison to incandescent or fluorescent light sources.[1]

GaN has a theoretically high breakdown voltage V_{br} due to its wide band gap which makes it ideal for PIN- and Schottky rectifiers. The breakdown is caused by impact ionization, for wide band gap semiconductors a larger electrical field is needed to generate carriers due to electrons colliding with lattice atoms.

High electron mobility: Because of its high electron mobility and high saturated drift velocity the material allows a high switching frequency, therefore switching power supplies using GaN reaches higher efficiency leading to lower losses.
Because of their accessible high frequency and high power performances GaN High Electron Mobility Transistors (HEMTs) attracted attention. HEMTs make use of a two-dimensional electron gas (2DEG) formed between an AlGaN/GaN surface.[1]

Profitability: The availability of heterostructures is the reason why III/V semiconductor are superior to other wide band gap materials like silicon carbide (SiC), even though the growth and processing technology for SiC is more sophisticated. The support of heterostructure technology lead to the possibility of making quantum wells, modulation-doped heterointerface and heterojunction structures. Furthermore heteroepitaxy provides the possibility of fabricating GaN on industrial Si wafers for example, therefore a high throughput can be reached.

According to IMS Research (April 2013)[2] the worldwide revenue from sales of SiC and GaN power semiconductors is expected to rise from \$143 million in 2012 up to \$2.8

---

[1] S.J. Pearton, F. Ren, A.P. Zhang, K.P. Lee, „*fabrication and performance of GaN electronic devices* “; Materials Science and Engineering, Reports: A Review Journal, 55 (2000)

billion in 2022. SiC is currently dominating the high voltage marked with the high voltage Schottky diode as its best-selling device. The dominance of SiC is predicted to decline when low priced GaN diodes become available. High voltage SiC Schottky diodes are approximately 10 times more expensive than high voltage Si bipolar diodes. When low priced GaN diodes become available, the replacement of bipolar diodes by Schottky diodes could be driven by high voltage GaN Schottky diodes with performance levels similar to SiC diodes but the low cost levels of Si bipolar diodes.

---

[2] *„Silicon Carbide and Gallium Nitride Power Semiconductors - World - 2013 “*; IMS Research marked analysis, (2013)

1.2 GaN growth challenges

Growth research on III/V nitrides started in the early 1960s, their development was far behind the Si and GaAs semiconductor development, since Si and GaAs is easier to grow. But while the promising properties of nitrides are just about to unveil, Si and GaAs have already reached their theoretical limits.

A big challenge is that homoepitaxial growth is not possible, due to the unavailability of growing large (>1cm) GaN single crystal thin films. The reason for this challenge can be found in its high melting point and extremely high decomposition pressure, hence conventional growth techniques like the Czochraslski or Bridgman process, with which Si and GaAs are grown, can't be used.

Therefore heteroepitaxial growth is necessary with the difficulty to find a suitable substrate with a low thermal expansion as well as a low lattice mismatch with the GaN crystals. Heteroepitaxy of GaN on sapphire or 6H-SiC substrates result in various defects in the GaN, mainly threading dislocations, which density ranges between 10^9 and 10^{10} cm^{-2}. Whereas the dislocation density of homoepitaxial grown GaAs ranges between 10^2 and 10^4, the dislocation density of homoepitaxial grown Si is almost 0. With a lattice misfit of 3.5% 6H-SiC would be a promising substrate material, however sapphire with a lattice mismatch of 13.8% is used usually due to its lower price. Si seems to be an attractive alternative substrate, since Si wafers are cheap and the crystal quality is the best compared to other substrates. Because of its lattice mismatch of 17% and a different thermal expansion coefficient GaN grown on Si wafers has with threading dislocation densities of 10^8 and 10^{12} cm^{-2} a much lower quality compared to sapphire and 6H-SiC so far. In (fig. 1.1) dislocations in a heteroepitaxial grown GaN can be seen.[4]

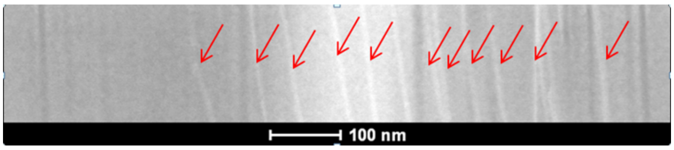

Figure 1.1: Dislocations [3]

---

[3] unpublished image by courtesy of Zhaoxia Bi

[4] L. Liu, J. Edgar, „*Substrates for gallium nitride epitaxy* “; Materials Science and Engineering R 37, 61-127 (2002)

The most suitable substrate to grow GaN on would be LiGaO_2, but its thermal stability cause problems for the growth conditions. The lack of suitable bulk materials is drastically limiting GaNs full potential, its promising theoretical properties discussed in fig. 4.5b are hardly reached therefore.

Dislocations introduce steps in the band gap, affect the optical and transport properties of the GaN and act as coulomb scattering centers, which leads to a reduced device lifetime. Threading dislocations are furthermore limiting the V_{br} (break down voltage) to about 600V. By decreasing the defects in the crystal a much higher V_{br} could be achieved theoretically, superior to silicon or silicon carbide.

Metal organic vapor phase epitaxy (MOVPE, appendix A.1) became the leading technique to produce III/V nitrides nowadays, other techniques to grow GaN are hybrid vapor phase epitxy (HVPE) and molecular beam epitaxy (MBE).[1] [5]

Another challenge in the growth process turned out to be the relatively high n-type doping of the non-intentionally doped GaN grown on the substrate. P-type doped GaN was not achievable for a long time, the reason is that out of only one-hundredth of the acceptor impurity concentration a hole is generated by ionization at room temperature, because the ionization energy is too low at room temperature. This means that the residual n-type doping should be as low as possible in order to achieve p-type doping. Oxygen is assumed to be the most likely source of the residual n-type doping. Magnesium is often used for p-type doping, but Mg-H complexes are built during growth, which passivates the acceptors. An additional activation process, like thermal annealing or low-energy electron beam irradiation treatment (LEEBI) is required in order to break the Mg-H bond and thus get the full electrical activity of the acceptors back.[6]

1.3 GaN quality improvements

It turned out that an increase of the grown GaN layer thickness don't lead to a significant lower number of threading dislocations in the GaN.[5]

---

[1] S.J. Pearton, F. Ren, A.P. Zhang, K.P. Lee, *„Fabrication and performance of GaN electronic devices“*; Materials Science and Engineering, Reports: A Review Journal, 55 (2000)

[5] B. Beamount, Ph. Vennegues, P. Gibart, *„Epitaxial Lateral Overgrowth of GaN“*; physica status solidi (b), 227 (2001)

[6] Pierre Gibart, *„Metal organic vapour phase epitaxy of GaN and lateral overgrowth“*; Reports on Progress in Physics, 667 (2004)

A way to decrease the dislocation density to the low $10^8\ cm^{-2}$ is to grow an appropriate buffer layer, which purpose is to accommodate the lattice mismatch to some extent before depositing the actual GaN layer.

For further reduction of the dislocations the epitaxial lateral overgrowth (ELO) technology has been developed. In this technique a dielectric mask is used to cover wide areas of a epitaxial grown GaN layer surface, which has a high dislocation density. The GaN growth will be started again afterwards, with the result that deposition occurs only at the mask openings but not on the dielectric mask, this type of growth is also known as selective area epitaxy (SAE) and should filter the defects. Lateral extending (wings) of the deposited GaN at the mask openings forms a new GaN layer covering the dielectric mask. The mask prevents the threading dislocations to extend into the new GaN layer above, only at the mask openings the dislocation density is the same as in the initial GaN layer.

There are two different types of the ELO technology, the simpler one is called one-step-ELO and was basically described above. The one-step-ELO leads to a GaN layer, which can be distinguished in a high dislocation density area above the mask openings and a low dislocation density GaN between the openings above the mask. This allows fabricating low dislocation density GaN devices between the mask openings.

The second main ELO technology uses also a dielectric mask and is called two-step-ELO, where triangular stripes are grown above the mask openings, by modifying the growth conditions in a way the vertical growth is faster than the lateral growth. The threading dislocations in the mask openings are bent by $90\,^{\circ}$ when they reach the facet of the triangular GaN stripes, so that the dislocations are propagating parallel to the dielectric mask below. In the second step the growth conditions are modified again in a way the lateral growth is much faster than the vertical growth. The second step is finished when the GaN is covering the whole surface. In the two-step-ELO defects can be found only at the boundaries where two GaN wings from neighbor mask openings meet.

The ELO technology enables high quality GaN with threading dislocation densities in the mid $10^6\ cm^{-2}$ but even the ELO quality GaN suffers on too much defects for devices like laser diodes.[6]

1.3.1 Nanowire based GaN

A Team around Qunano AB and Lunds University developed a new technique to produce high quality GaN, which allows to produce high quality devices based on GaN [7]. As substrate material Si had been chosen because of its low cost. An epitaxial GaN buffer layer had been grown on the substrate. This buffer layer exhibits a high dislocation density, due to the lattice mismatch as well as the different thermal expansion coefficient between the diamond cubic Si-Crystal structure and the wurtzite crystal structure of GaN. Subsequently a silicon nitride dielectric mask with an array of pinpoint openings is deposited on top of the Si buffer layer. As described in the previous section 1.3, re-growth occurs only in the pinpoint openings, which refers to as selective area epitaxy (SAE), see section 1.3 [8] [9].

Apparently threading dislocations don't propagate into the nanowire geometries (fig. 1.2) [10], which are fabricated by MOVPE, see also appendix A.1. Therefore GaN nanowires are grown out from the pinpoint openings, a schematic of the structure can be seen in fig. 1.3a. After the nanowire is fabricated, the GaN is grown laterally.

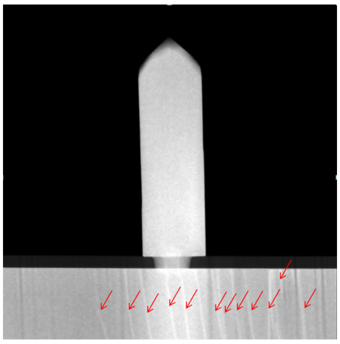

Figure 1.2: GaN buffer with dislocations. Dislocations don't grow up into a nanowire [11]

Diffusing molecular species prefer to integrate at different crystallographic positions, which leads to different growth rates on different crystallographic planes, this corresponds to anisotropic crystal growth. The longer the lateral growth lasts, the wider

---

[7] Patent: WO 2013121289 A2, QuNano AB, *„Gallium nitride nanowire based electronics“*; 12.2.2013

[8] Kihyun Choi, MunetakaArita, YasuhikoArakawa, *„Selective-area growth of thin GaN nanowires by MOCVD“*; Journal of Crystal Growth 357 ,58–61 (2012)

[9] Stephen D. Hersee, Xinyu Sun, Xin Wang, *„The Controlled Growth of GaN Nanowires“*; Nano Letters Vol. 6, No. 8, 1808-1811 (2006)

[10] Stephen D. Hersee, Ashwin K. Rishinaramangalam, Michael N. Fairchild, *„Threading defect elimination in GaN nanowires“*; Cambridge Journals Material Research, Vol. 26, No. 17; 2293 (2011)

[11] unpublished image by courtesy of Zhaoxia Bi

these structures will become, from the initial nanowire (fig. 1.3a), over a small pyramid-hat on top of the nanowire (fig. 1.3b) until finally a full pyramid is formed (fig. 1.3d), with a size depending on the growth conditions but roughly 1 μm high and 1 μm wide. Usually the growth is stopped after structures comparable to fig. 1.3c are formed.
As an effect of the nanowire being free from threading dislocations, the lateral grown GaN is dislocation free as well. Therefore hexagonal high purity GaN structures, based on nanowires are formed with this growth technique.

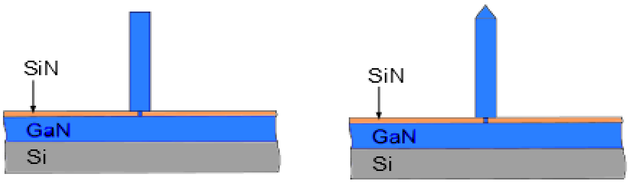

(a) Nanowire **(b)** pyramid-hat

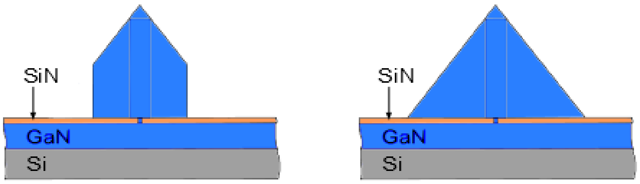

(c) common shape **(d)** full pyramid

Figure 1.3: Pyramid growth

These structures have a hexagonal top view, such as the wurtzite crystal structure of the GaN (fig. 1.4a).

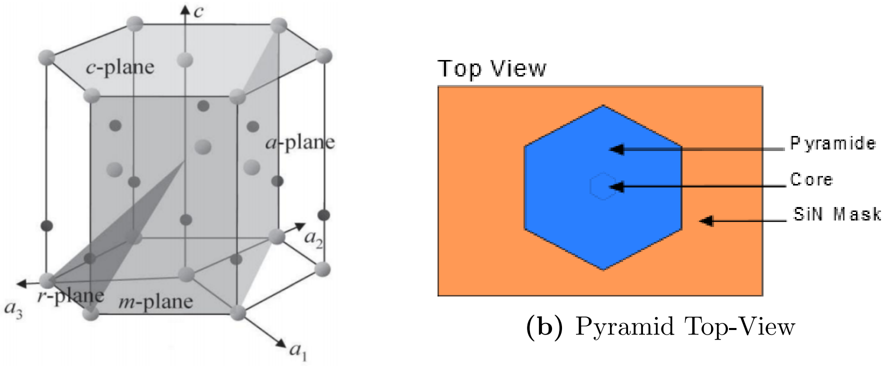

(a) Wurtzite Crystal[12]

(b) Pyramid Top-View

Figure 1.4

The pyramids will be flattened by a thermally assisted ”in situ” etch step and form a planar c-plane on their tops. In this process the material diffuse from the top to the side facets, the m-plane (fig. 1.5), supported by high temperatures. The process is similar to an annealing process (see appendix A.2) but used to flatten the pyramid.

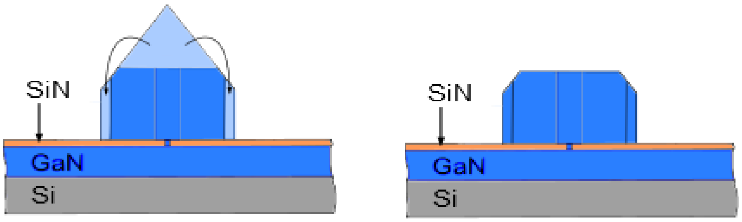

(a) **(b)** flattened pyramid

Figure 1.5

1.4 Aim

In order to develop electronic devices fabricated of nanowire based GaN platelets it is crucial to develop a technique to determine the carrier concentration and the carrier mobility of one single GaN platelet. Four Probe- and Hall measurements would be a possibility to measure these parameters. The aim was therefore to develop a viable contacting process for a single nanowire based GaN platelet to enable 4-probe measurements and to investigate if Hall measurements are possible for future investigations.

1.5 Sample A

Since this is the most investigated sample during the work, a closer look will be taken on it.

The whole ”pyramid-roof” was flattened away by the thermally assisted ”in situ” etch step. The material diffused from the c-plane to the m-planes of the structure where new slopes were formed. (fig 1.6a).

An undoped layer followed by an Silicon doped (nominally 1e18 $\frac{1}{cm^3}$) layer was grown on top of the c-plane afterwards. The growth time of the undoped layer was 600s and 400s for the doped layer, which led to heights of 56nm for the undoped- and 46nm for the doped layer, respectively.

---

[12] J. H. Ryou et al., „*Control of quantum-confined Stark effect in InGaN-based quantum wells* “; IEEE of Selected Topics in Quantum Electronics, 15, 1080 (2009)

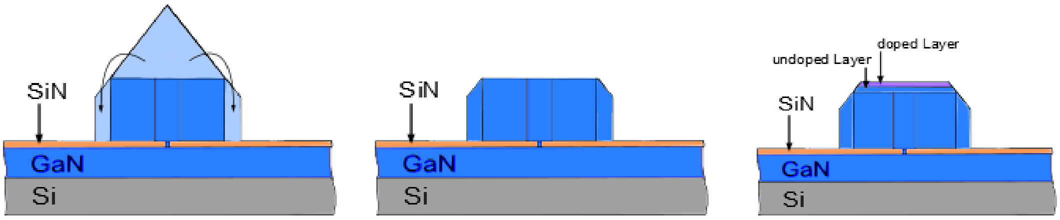

(a) sample A: thermally assisted ”in situ” etch **(b)** sample A flattened **(c)** sample A doped

Figure 1.6

In the SEM (Scanning electron microscope) image of the sample A only one contrast change is visible, it indicates the transition from the initial c-plane to the region containing both the undoped and doped layers. Hence the top region after the contrast change combines the doped and undoped layer, see fig. 1.7 and fig. 2.25b.

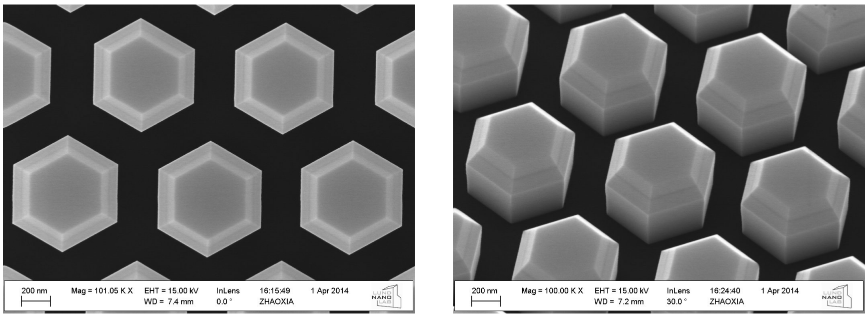

(a) Top view **(b)** 30 ° view

Figure 1.7

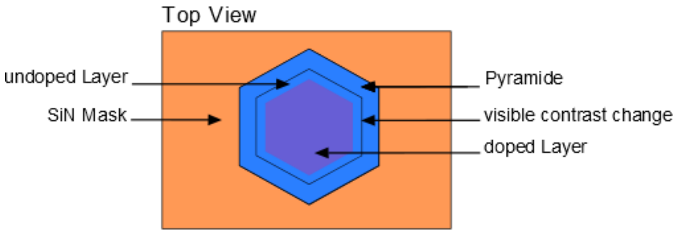

Figure 1.8: Top view shematic

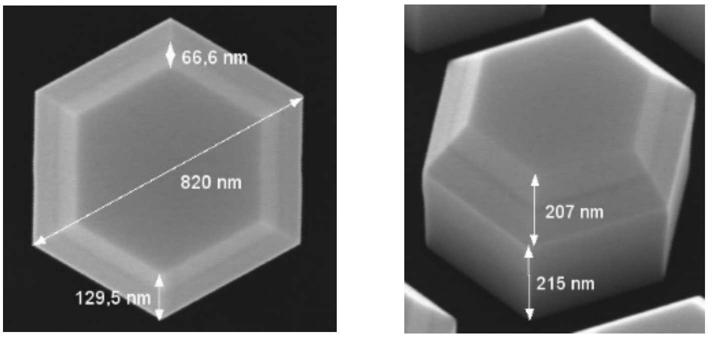

(a) Top view **(b)** 30 ° view

Figure 1.9: Dimension of sample A

The dimensions of sample A was measured in the SEM image shown in fig. 1.9. The Diameter of the platelet is 820 nm and the height turned out to be 640 nm, which was calculated under consideration of all angles in the image above.

1.6 Sample B

This sample differs from sample A there in that there is no doped layer above the undoped layer. This sample was used to give the conductivity of undoped GaN and to confirm that it is sufficiently resistive to be used as an insulation layer to characterize a doped layer upon it by Hall measurments.

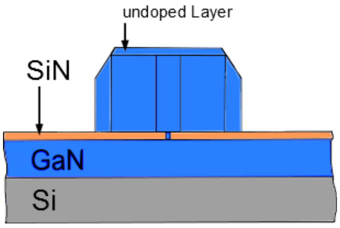

Figure 1.10: illustration of sample B

Even the undoped layer has an unintentional background doping, caused by impurities during the growth process. The value of this background doping for the investigated platelets is unknown. Other research groups have shown backrground dopings below $5 \cdot 10^{16}\ \frac{1}{cm^3}$ for GaN grown with MOCVD [13] [14].

---

[13] S. Strite and H. Morkoc, *„GaN, AIN, and InN: A review“*; American vacuum society, 1237 (1992)

[14] J. C. Zolper, R. G. Wilson, S. J. Pearton, and R. A. Stall, *„Ca and O ion implantation doping of GaN“*; Applied Physics Letters, 68, 1945 (1996)

2

Contact processing

In order to contact one single GaN platelet out of an array of GaN platelets several process steps were necessary. After a couple of iterations a viable process was found, which will be explained in this section.

2.1 Process overview

An overview of the contact process will be presented before details on each step are given.

1. **Sacrificial layer**

   The very first step was to cover the platelets with a thin sacrificial layer (fig. 2.1) to protect the structures from oxidation or other process steps such as oxygen plasma which is known to affect the GaN surface properties.

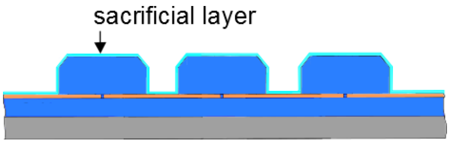

Figure 2.1: Sacrificial Layer

2. **Cover layer**

   It was necessary to cover the sample with a resist layer in order to isolate the platelets from the final contacts. In fig. 2.2 the cover layer is shown as a dark blue layer embedding the platelets. The photoresist Shipley S1805 was chosen as it is easy to permanent-bake it and it forms a relatively stable base for subsequent bond pads.

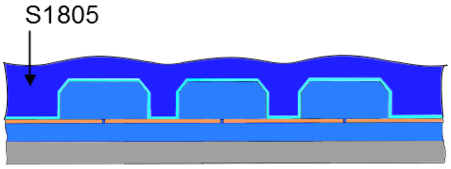

Figure 2.2: Cover Layer

3. Bond pads

Bond pads allow contacting the nanoscale structures to external devices, such as a probe station or an integrated circuit socket. Because the final wires which are bonded to a platelet are to small for being used by external equipment, bigger structures which serve as an interface are needed. These so-called bond pads need to be connected to the four small platelet-contacting wires. The available photolithography mask consists of 48 bond pads hence 12 platelets can be bonded per sample (fig. 2.3), because four contacts are needed per platelet, in order to perform 4-probe and Hall-measurments on them.

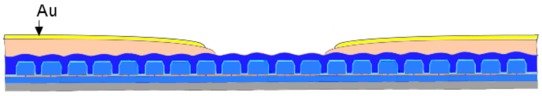

Figure 2.3: Bond Pads

4. Alignment marks

The contacts need to be well aligned to the platelets, which is very difficult because of the small dimensions of the structures. A way to achieve accurate alignment is to use well defined marks. Therefore four small metal crosses need to be added per device to the structure by EBL (Electro-Beam Lithography, appendix A.9). The alignment marks are used to align EBL patterns, which are drawn outside of the lab, to the sample by matching the crosses on the pattern to the alignment marks on the sample.

5. Mapping

High resolution SEM images of the EBL write-fields with the platelet of interest need to be taken. They will serve as templates to design the necessary EBL patterns for each write-field individually.

6. **Creating a hole**

   One single GaN platelet needs to become accessible for metal contacts. It is therefore necessary to expose a single platelet by removing the insulation layer in the immediate vicinity of the platelet, fig. 2.4.

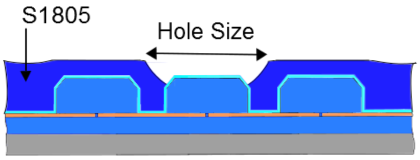

Figure 2.4: Hole above platelet

7. **Contacts**

   Finally the uncovered platelet needs to be contacted by four metal wires which are connected to the bond pads at the other end, see fig. 2.5. This structure forms a device which allows to measure and investigate the behavior of a GaN platelet.

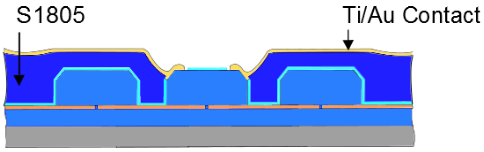

Figure 2.5: Contacts

2.2 Sacrificial layer

2.2.1 ALD

With help of an ALD-system (Atomic Layer Deposition, see also appendix A.3) Savannah-100 from Cambridge nanotech a thin layer of ZnO was deposited, see fig. 2.6. A preinstalled recipe was in use, the pulse time for ZnO and the second precursor, H_2O was 15 ms. The pump time in between these pulses was set to 5 s. The process was iterated for 80 cycles at a temperature of 175 °C in the reaction chamber.

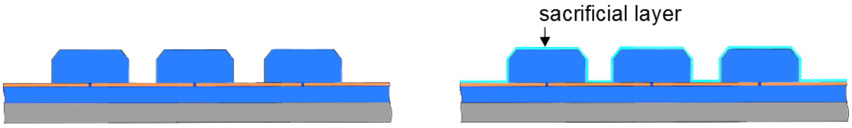

(a) sample before ALD

(b) sample covered with a thin ZnO layer

Figure 2.6

2.2.2 Ellipsometer

A Woollam M2000VI ellipsometer (appendix A.4) was used to measure the thickness of the ZnO on a dummy sample which was added into the ALD reaction chamber together with the proper sample. The reference sample was a planar one inch Silicon wafer. For sample A the measurement gave a thickness of 138 Å with reasonable error tolerances.

2.3 Cover layer

2.3.1 Spinning

A Shipley resist s1805 was applied on the sample using a Spinner (appendix A.5) PRIMUS SB15/STT15 at 2000 rpm (rotations per minute) for 30 seconds (fig. 2.7). Which led to a thickness of approximately 650 nm according to the datasheet[15]. In fig. 2.7b can be seen that the actual thickness was a bit higher, that's because the structured surface of the sample affected the centrifuge behavior of the liquid resist.

---

[15] http://nanofab.ece.cmu.edu/resources/s1800seriesDataSheet.pdf

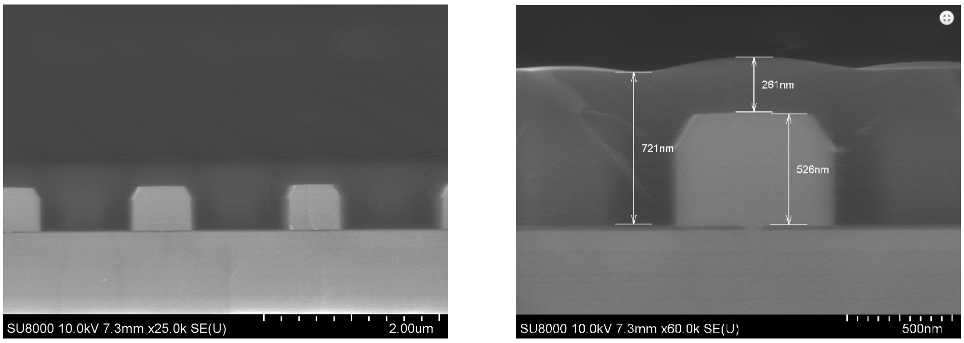

(a) (b)

Figure 2.7: Cross section SEM of a resist covered dummy sample

2.3.2 Hardbake

The covered sample (fig. 2.8) was prebaked on a hotplate at a temperature of 250 °C for 15 minutes to stabilize the resist by desorb most of the water of the solvent. The backside of the sample was cleaned with acetone after spinning, to make sure that the sample won't stick to the hotplate.

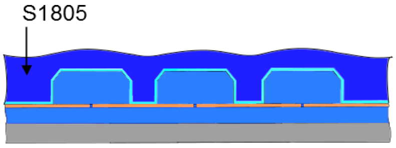

Figure 2.8: Resist covered sample

2.4 Bond pads

2.4.1 Bond pad lifting layer

A lifting layer was spun on the sample, upon which the bond pads were attached later. This lifting layer serves as a proper electrical insolation of the platelets, since the Shipley resist covering the platelets is too thin to ensure insulation. Furthermore it helps to protect the platelets from mechanical stress caused by external equipment like needles from a probestation. A Shipley resist S1818 was used with 3000 rpm for 60 seconds. The sample was baked on a hotplate for 90 seconds at 115 °C after cleaning the backside with acetone to remove residues from the spinner.

2.4.2 Strip exposure

A strip of the lifting layer in between the future bond pads, where the platelets were contacted later needed to be removed, otherwise there would have been to much resist to etch away above the platelet of interest. The etch step will be described later at section 2.7 and is necessary to expose one single GaN platelet.

A photolithography step (appendix A.6) is needed in order to remove this strip. Therefore a Soft UV contact mask aligner MJB4 was used. The available mask contained 10 μm thick strip patterns, which are projected on the sample by UV-light. The mask was aligned above the samples in a way to expose areas where platelets are grown. The resist S1813 is a positive photoresist and will be removed at the exposed areas after developing, due to a chemical change in the resist caused by the UV-light. After a look at the datasheet [15] an exposure time of 10 seconds was chosen, which led to a dose of $210\frac{mJ}{cm^2}$ for this mask aligner.

2.4.3 Strip development

In order to remove the exposed strip, the sample needs to be developed. Therefore the sample was put in a beaker filled with the developer MF319 for 70 seconds. Afterwards it was rinsed with deionized water to remove developer and resist residues.

2.4.4 Hardbake

To keep these new structures that can be seen in fig. 2.9 permanent, hard baking on a hotplate at 250 °C for 15 minutes was necessary.

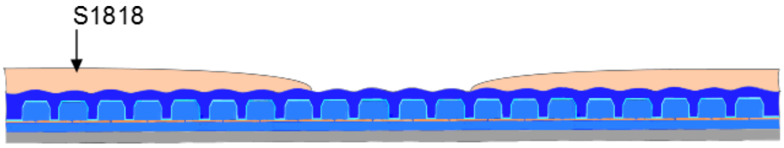

Figure 2.9: hardbaked lifting layer

2.4.5 Lift-off stack

The next step was to deposit bond pads on the sample. For this purpose, a lift-off stack consisting of Lift-Off Resist (LOR) together with Shipley S1813 was defined, see fig. 2.10. Both resists were spun on the sample with 3000 rotations per minute for 60

---

[15] http://nanofab.ece.cmu.edu/resources/s1800seriesDataSheet.pdf

seconds. The first layer (LOR 30B) was post baked for 5min at 165 °C after spinning and cleaning the backside, A Shipley S1813 was used for the second layer, post baking took place at 115 °C for 90s, identically to the lifting layer earlier.

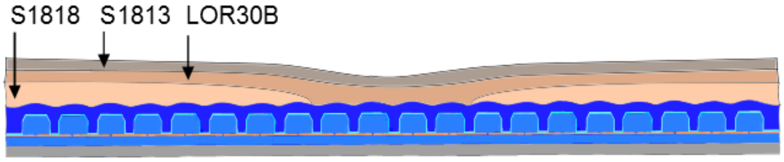

Figure 2.10: lift-off-stack

2.4.6 Pad exposure

It turned out to be helpful to carefully remove the edge beads, caused by the spinning, with a scalpel. Otherwise, the mask aligner can't achieve perfect alignment since the sample would move when it comes in contact with the mask. As mentioned earlier a bond pad mask consisting of 24 pads on each side will be aligned in a way that these 24 pads are placed symmetrically to the trench developed before in section 2.4.3. The exposure time was 8,6 s, which led to 180.6 $\frac{mJ}{cm^2}$, an appropriate exposure dose according to the datasheet, fig. 2.11.

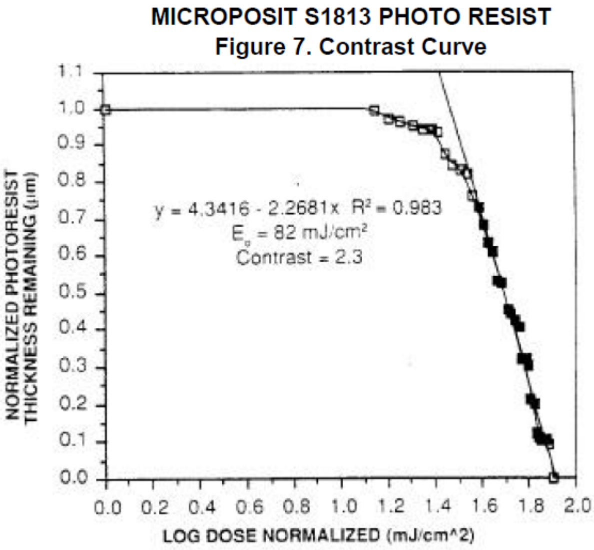

Figure 2.11: [15]

2.4.7 Pad development

Again the developer MF319 was in use. In the double layer development process, the shipley resist on top was developed first, and subsequently the LOR was developed, both in a single development step. The LOR30B is removed by the developer either way, exposed or unexposed, the unexposed Shipley on the other hand remains. Therefore a so-called undercut (fig. 2.12) was formed since there was less of the LOR30B than of the Shipley resist remaining on the sample. Afterwards the sample was rinsed with deionized water. The sample was dried with a nitrogen gun subsequently.

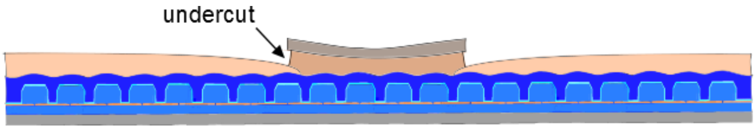

Figure 2.12

2.4.8 Preening

In order to remove organic contamination, like resist residues from the surface, a plasma asher (appendix A.7) was in use for 30s at a pressure of 5mbar. The used plasma preener was a modified microwave. The sample was covered with a small Faraday cage to slow down the ashing rate, otherwise the ionized particles would have hit the sample directly without slowing down.

2.4.9 Pad deposition

A Pfeiffer Classic 500 Evaporator (appendix A.8) was used for the metallization of the bond pads. The sample was amounted upside down in the top of the vacuum chamber, which was pumped down for two hours to a pressure of $5 \cdot 10^{-7}$ mbar. The desired metals, in this case titanium and gold, were placed in special metal boats that can stand high temperatures. These boats were heated up until the metals in them were melting and evaporated to the top of the chamber where they ended up on the sample. The evaporation process is highly anisotropic due to the low pressure in the chamber. First a 5nm thick Ti-layer was deposited to enable proper adhesion conditions for the following Au-layer. 225nm of gold were deposited for contacting the sample with external equipment (fig. 2.13).

---

[15] *„http://nanofab.ece.cmu.edu/resources/s1800seriesDataSheet.pdf"*

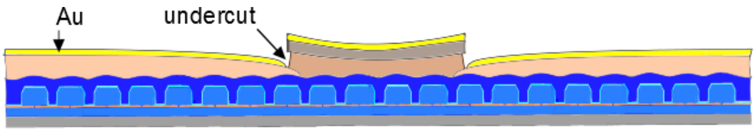

Figure 2.13: evaporation

2.4.10 Lift-off

The sample was inserted into a beaker of a remover 1165 for approximately 30 minutes. The beaker was placed on a hotplate at 80 °C in order to support the lift-off process. To scratch the evaporated metal along the edges turned out to be helpful for the process as well. Afterwards the sample was rinsed with deionized water, to get rid of remover residues and finally dried with a nitrogen gun. Because of the undercut in the lift-off stack, the metal was not covering the whole sample and therefore metal areas were not connected to each other (see also fig. 2.13). The solvent washes the lift-off stack together with the material covering it away. The metal stays only at areas where the lift-off stack was removed by the photolithography step earlier (fig. 2.14).

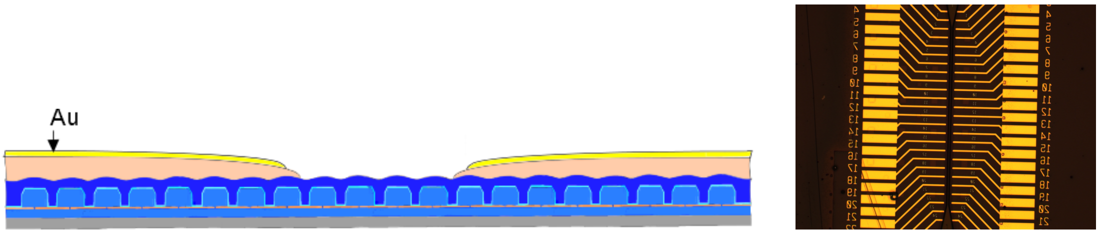

(a) After lift-off

(b) Top view optical microscope image

Figure 2.14

2.5 Alignment marks

2.5.1 Resist for EBL

A solvent, called Zep 520A7 was spun on the sample at 5000 rpm. Afterwards the sample was baked on a hotplate at 180 °C for two minutes. The resist layer was necessary for the following lithography step, Zep was developed for Electron Beam Lithography. A scalpel instead of acetone was used to clean the backside to remove residues. Evaporated acetone could harm the resist on top of the sample otherwise. The boiling point of acetone is at 56 °C and evaporates at room temperature quite quickly.

2.5.2 Alignment marks exposure

A Raith 150 was used to perform the EBL steps (see also appendix A.9). The sample has to be mounted absolutely planar to the holder for a proper alignment and focus of the sample. The holder moves the sample to the operating position after pumping the load lock chamber down to a vacuum level. The pattern for the alignment marks was already installed on the computer, which controlled the EBL equipment. The Dose for area exposure was set to $65\frac{\mu C}{cm^2}$ and for line exposure to $260\frac{\mu C}{cm}$. Four steps need to be done before the e-beam can start writing the patterns on the sample. These four procedures are:

Angle Alignment The Raith 150 does not know in which angle the sample was mounted to the holder, therefore one has to choose two points which should be on the same height, two points at the upper edge of two symmetric bond pads for instance and define these points to be on the same height. The greater the distance between these points, the more precise will be the alignment.

Focus In order to align to small structures one has to focus properly. Therefore a spot will be burned into the surface of the sample with the e-beam. The next step is to iterate focus on the burned spot and get rid of x- and y-stigmatism over and over again until the result is satisfying.

Write-field Alignment A Write-field is the rectangular area of the target sample where the pattern will be written on. In order to align this field, a small well defined structure need to be found and focused on, which position has to be corrected three times in the program for the Raith 150. After performing this writefield alignment the Raith 150 knows where to write the pattern. The smaller the structure, the more precise the alignment will be.

Calculation of the Beam-dose First, the current of the beam needs to be measured. Therefore the beam will be moved to a faraday cup where the current can be measured. The dose $D = I * t$ will be set and the program calculates the time needed to achieve the desired dose.

2.5.3 Alignment marks development

To develop the Zep-resist the sample was inserted into a beaker filled with O-Xylene for five minutes. The exposed parts of the resist were washed away. Instead of water, isopropanol was used to rinse the sample to get rid of residues before the surface was dried with a nitrogen gun.

2.5.4 Preening

The same Process for the same reason as explained in section 2.4.8.

2.5.5 Alignment mark deposition

See also: section 2.4.9. This time 5nm of Titanium and 30nm of gold were deposited. The Alignment Marks were not supposed to be contacted nor to transport electrical current, hence there was no reason to evaporate a thick gold layer. The Lift-off process did benefit from a thinner gold layer as well, since the chance was higher that gold areas are broken at edges to gaps, caused by different height levels beneath.

2.5.6 Lift-off

See also: section 2.4.10. Additionally the beaker with the sample in it, needed to be put into a supersonic bath for 30 seconds at the second lowest power. The supersonic bath includes a metal cage hanging in deionized water. The cage is open on the top-side and vibrating with a high frequency. The energy of the vibrations is carried by the water and forwarded to the beaker positioned on the cage. These vibrations support the lift-off process but the power should be chosen carefully, if the power is too high wanted structures could be destroyed. An optical image of the alignment marks after the lift-off process can be seen in fig. 2.15.

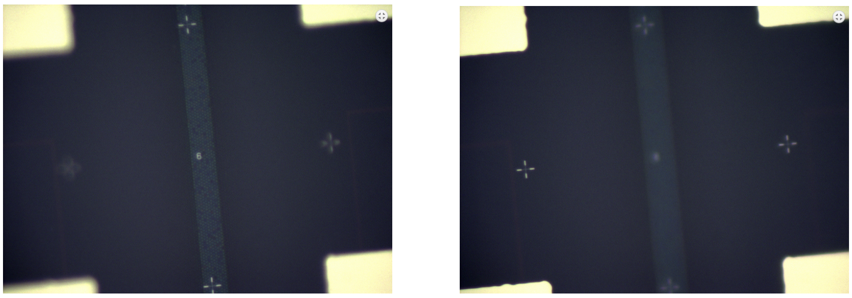

(a) focused on trench **(b)** focused on lifting layer

Figure 2.15: Alignment Marks of Write-field 6

2.6 Mapping

In fig. 2.15 Write-field six of sample A is visible, to design proper individual EBL patterns for the final contacts, high resolution pictures were taken of all Write-fields with a SEM. In fig. 2.16 two out of twelve write field images are shown, which were taken for each sample. They served as templates to design the contacts and a hole-mask on.

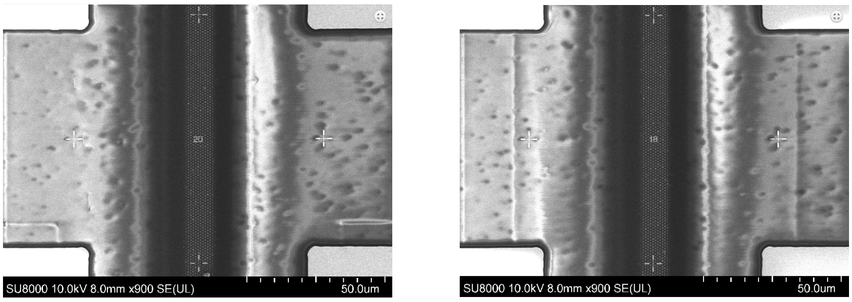

(a) Write-field 20 **(b)** Write-field 18

Figure 2.16: Mapping

2.7 Creating a hole

2.7.1 Hole mask layer

With the help of the mapping images a pattern was designed, individually for the target-platelet. This pattern includes a hole and the final contacts, defined by an available MATLAB-program. The contacts and holes were not exposed at the same time. The contacts will be exposed at a later point instead.

The hole-mask consisted of a PMMA-A8 and the desired thickness is about 600 nm. As

the hole-mask layer served as a sacrificial etching buffer coating, a certain thickness is needed. According to the datasheet [16] the PMMA layer was spun on with a duration of 3000rpm for one minute followed by baking at, 180 °C for five minutes to achieve this thickness, see fig. 2.17.
Again a scalpel instead of acetone was used to clean the backside.

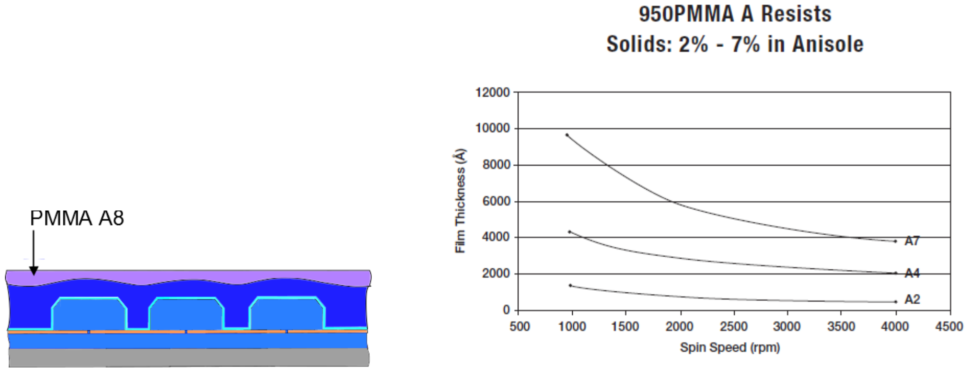

(a)

(b) PMMA thickness curve [16]

Figure 2.17

2.7.2 Hole exposure

Apart from using a different pattern and a higher dose ($225\frac{\mu C}{cm^2}$) the process was the same as explained in section 2.5.2. The EBL-mask was created with an available program based on MATLAB, the patterns were designed individually for each write field. The EBL-program allows exposing different layers of the pattern. The pattern for the holes were designed at the same time as the contact structures since they need to be well aligned to each other but they were created in different layers. That means it was possible to expose the hole-layer only and the contact layer at a later point. Since the alignment was difficult to perform and there are twelve write fields per sample, the holes were designed slightly different to each other in order to increase the chance of achieving some well aligned holes in the development phase of the process. One half of the holes had a diameter of 0.35 μm and the other half 0.38 μm. Furthermore the lentgh of the contacts above the holes were increased for every other write field.

---

[16] http://microchem.com/pdf/PMMA_Data_Sheet.pdf

2.7.3 Hole mask development

In order to remove the exposed PMMA, it was developed in MIBK:IPA 1:3 for one minute and rinsed with IPA afterwards, see fig. 2.18.

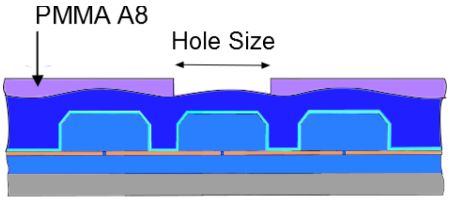

Figure 2.18

2.7.4 Hole ashing

A Table-top Reactive Ion Etching (RIE) system T2 from Trion Technology was used to etch down the surface of the sample (see also appendix A.10). The sample has to be inserted into a chamber, the desired gas, in our case oxygen, enters the chamber by opening the corresponding valve. Oxygen is flowing at the same time as a vacuum pump is operating. A throttle on the pump is regulating the pumping power so that the preset pressure is achieved. The chemical reactive plasma is generated by an electrical field afterwards. High energy ions will be created which will impact and react with the surface.

The maximum etch depth is depended to the original thickness of the hole mask layer. One would risk uncovering other platelets by etching too far down.

Therefore the etching behavior of the PMMA resist was investigated. This research has shown that the etch rate with the available equipment using oxygen as the gas is about 1,2nm per second for the PMMA but approximately 3 times slower for the resist beneath (see also, section 3.3). Considering the thickness of the shipley resist which is covering the platelets, a hole-depth of approximately 250nm - 300nm to uncover the top of the structures was the aim.

The pressure in the chamber was set to 300 mT, the RF power was set to 50 W and the gas flow of the oxygen was 15 sccm. The etch time was 925 seconds in total for sample A, interrupted by SEM inspections to check whether the platelet was uncovered enough in order to contact it. It turned out that the PMMA mask layer was thick enough and that the other platelets were still covered with enough resist.

2.7.5 Hole inspection

The etch-process was stopped after the surface looked satisfying at the hole inspection, see fig. 2.19. The platelets were still protected by the ZnO, which was added in the very first step. The platelets were therefore not attacked by the etch-process. Since the ashing is an isotropic process, which attacks side walls as well, the resulting hole was wider than the hole in the mask.

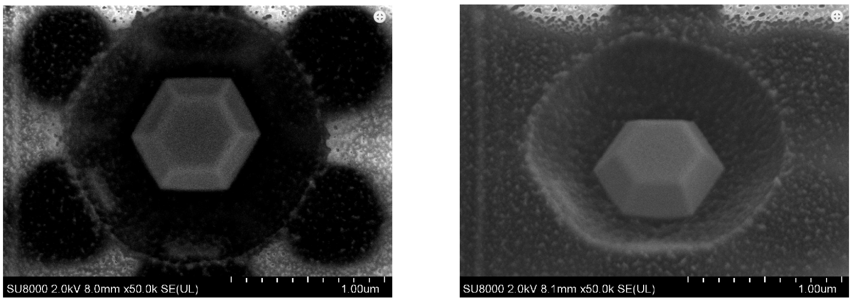

(a) Top View **(b)** 30 ° angle perspective

Figure 2.19: Hole inspection

2.7.6 Removing PMMA residues

Possible remained PMMA residues that survived the ashing were removed by putting the sample for 5 minutes into acetone, followed by rinsing it with isopropanol, fig. 2.20.

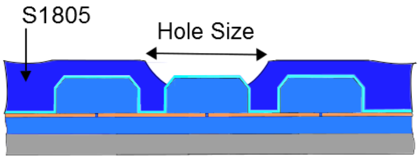

Figure 2.20

2.8 Contacts

2.8.1 Contact layer for EBL

Instead of the ZEP used in section 2.5.1, a PMMA 950 A5 was spun on with 5000 rpm and baked for 5 minutes at 180 °C (fig. 2.21), otherwise the process was the same.

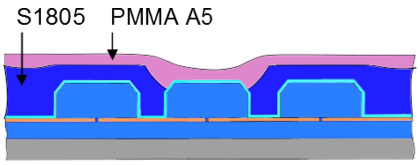

Figure 2.21

2.8.2 Contact exposure

See also, section 2.5.2. The contacts were exposed with an acceleration voltage of 15kV, an aperture of 30 μm and a dose of 300$\frac{\mu C}{cm^2}$.

2.8.3 Contact development

The PMMA was developed in MIBK:IPA 1:3 for 90 seconds and rinsed with IPA afterwards, the exposed PMMA was removed therefore, see fig. 2.22.

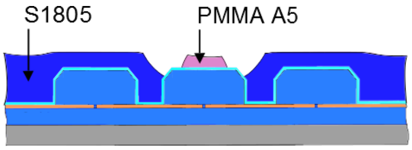

Figure 2.22

2.8.4 Preening

See: section 2.4.8.

2.8.5 Surface treatment

The surfaces of the platelets are still protected by the ZnO layer added by an ALD process. In order to contact the surface of the structures the ZnO had to be removed before metal was deposited.

Therefore the sample was inserted into a beaker filled with the acid, hydrogen chloride, diluted with deionized water (HCl:DIW 1:1) for 1 minute. The sample was rinsed with water afterwards.

Since the platelets were unprotected without the ZnO, there was a rush to pump the sample down to a low pressure in the vacuum chamber of the evaporator,in order to prevent oxidation.

2.8.6 Contact deposition

See also, section 2.4.9.

5 nm of Titanium and 150 nm of Gold were deposited on the surface, see fig. 2.23.

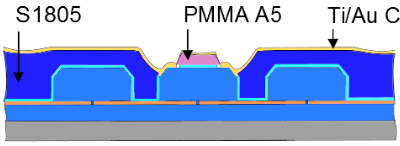

Figure 2.23

2.8.7 Lift-off

First, the edges of the sample were scratched with a scalpel along the edges in order to support the lift-off.

The sample was left in acetone for 3 hours before it was rinsed with isopropanol, see fig. 2.24.

Covering the beaker with a lid prevented the acetone from evaporation.

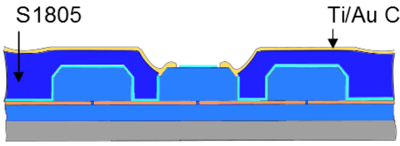

Figure 2.24

2.9 Final inspection

The three images below, fig. 2.25 were taken with a SEM and show the writefield 4 of the sample A.

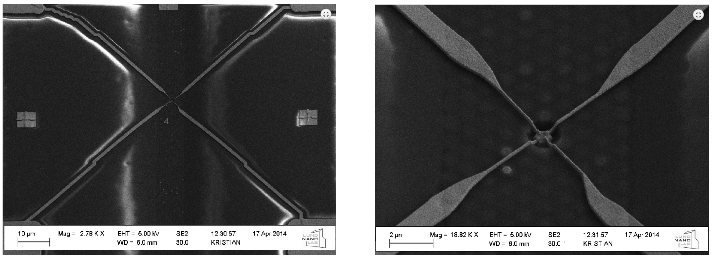

(a) A: Overview **(b)** A: Contacts

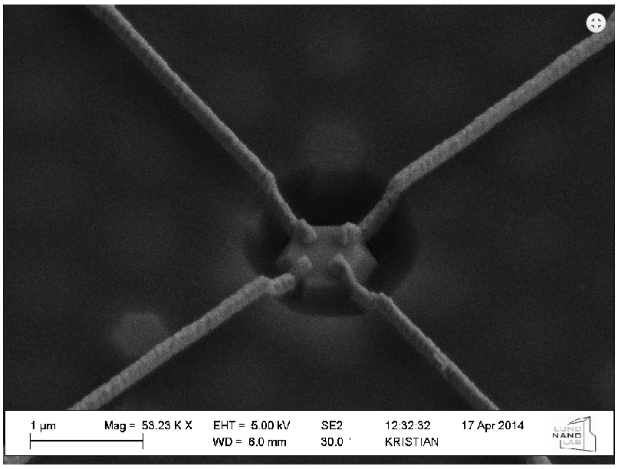

(c) A: Close Up

Figure 2.25: Final Inspection

Although the images looked promising, the measurements turned out to be surprisingly inconclusive, which motivated to take a closer look and inspect the surface another time.

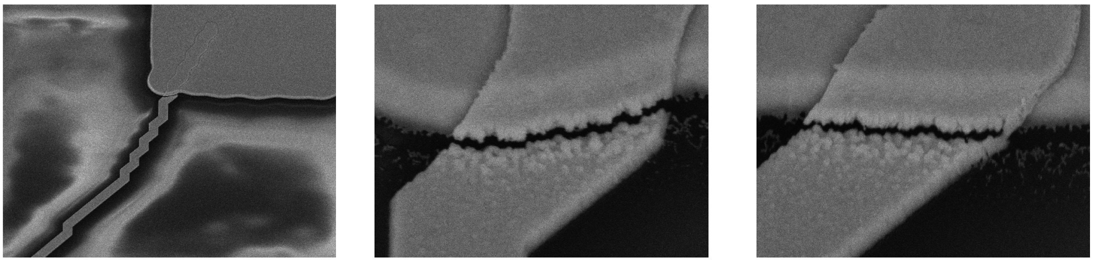

(a) **(b)** **(c)**

Figure 2.26: broken junction

Apparently the junctions between the bond pads and contacts were broken (fig. 2.26), due to the gap in the surface caused by the plasma etching. The step in the profile of the surface was too high and too steep to be covered with metal by the anisotropic Pfeiffer

Evaporator.

This was fixed very easily by repeating the steps from section 2.4.5 to section 2.4.10 by slightly misaligning the bond pad mask towards the contacts until all the broken junctions were covered with metal, see fig. 2.27. Placing the Bond Pad-process at the end as a final step instead of the beginning of the contacting process would have avoided this additional processing.

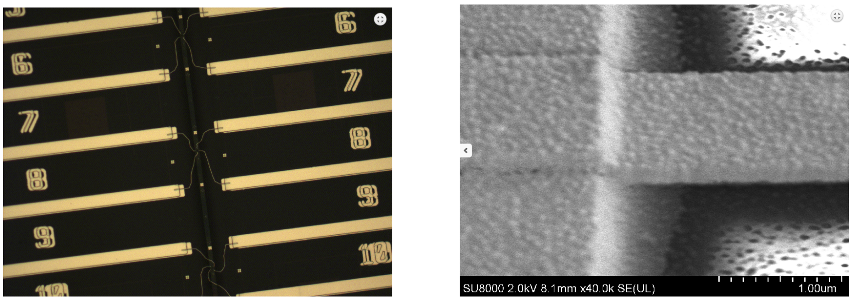

(a) Optical microscope image **(b)** SEM close up

Figure 2.27

3

Contact processing challenges and investigations

During the development of the contacting process a number of challenges occurred. Sometimes investigations were necessary in order to meet these challenges and to get a better understanding of the behavior for some processes.

3.1 Hard baked resist

The first explored challenge was that the permanent baked lifting layer was removed during the lift-off step after the bond pads were evaporated on the sample.

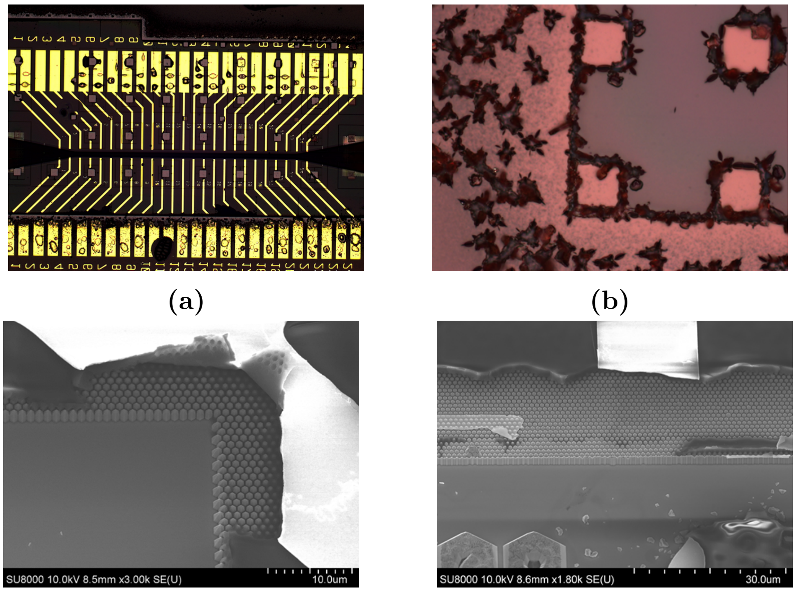

(a) **(b)** **(c)** **(d)**

Figure 3.1: Hard baked resist was removed

In fig. 3.1 one can see that the resist includeing the evaporated metal on it was removed, when there is an edge on the surface. It was a Shipley resist S1805, spun with 4000 rpm and was baked for 10 minutes at 200 °. The probe needed a supersonic bath to achieve a lift-off. Therefore it was assumpted that either the supersonic bath or the resist thickness caused the problem.

In order to find the cause of the problem, different thicknesses were spun on the sample. It turned out that the thickness had no big influence on the lift-off behavior.

Afterwards the sample was put inside a beaker filled up with isopropanol. That beaker was placed into the supersonic bath in order to investigate the threshold of the applied power that causes the damage seen in fig. 3.1. Surprisingly, even the highest power didn't harm the resist.

This means that the remover was the only remaining source for the issue. Since the remover was developed for this process, it was reasonable that the lift-off process wasn't the problem. It was suggested that something could have went wrong in the permanent baking of the resist.

Further tests with longer baking times at a higher temperatures led to the solution for the challenge. The resist didn't experience any harm when the hard baking took 15 minutes at 250 °. The baking time aswell as the temperature were too low to make the resist permanent. Ever since this parameters were used for the permanent baking processes.

3.1.1 Cross-linked PMMA

For the first samples the approach to contact the platelets was different. Instead of uncovering one platelet by etching a hole in an isolating layer it was tried to create four isolating paths from the bond pads to the platelet of interest. These paths were created in an EBL step (see also, appendix A.9). First a PMMA 950A6 was spun on with 4000 rpm and was baked for five minutes at $180\,^{\circ}$. This EBL resist was cross-linked by overexposing it, which means that the resist became permanent.[17] The used EBL-pattern was the same as the pattern used for the contacts, but slightly wider. The chosen EBL dose was 5000 $\frac{\mu C}{cm^2}$, which led to the best results in previous investigations. Afterwards the resist was developed in MIBK:IPA 1:3 for 60 seconds. The results can be seen in fig. 3.2.

[17]

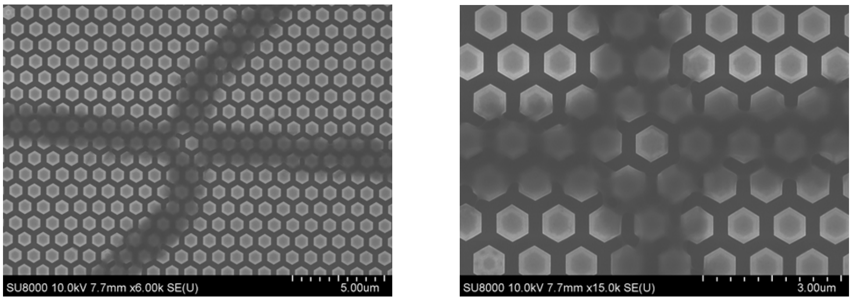

(a) **(b)**

Figure 3.2: SEM images of crosslinked PMMA

The actual contacts were created on top of the cross-linked PMMA in the same way as described in section 2.8. The results can be seen in fig. 3.3.

---

[17] M. A. Mohammad, M. Muhammad, S. k. Dew, M. Stepanova *„Fundamentals of Electron Beam Exposure and Development “*; Springer, 2012

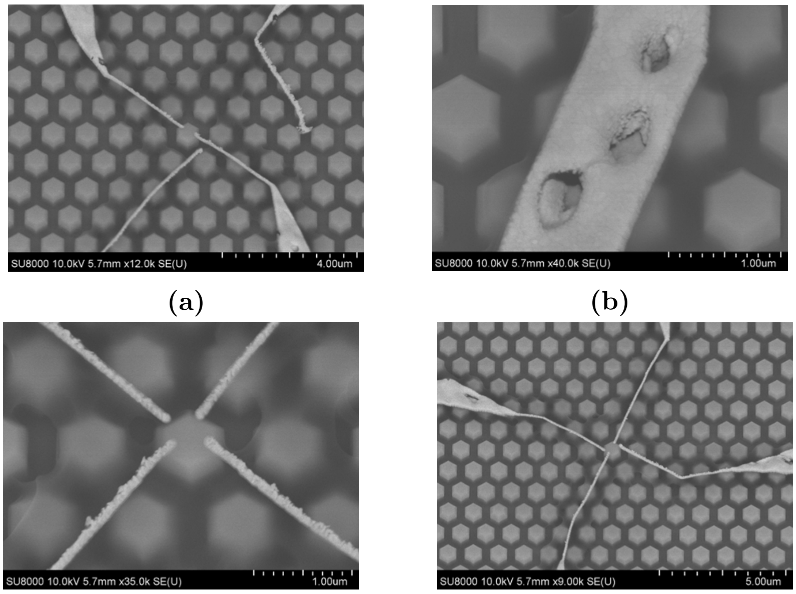

(a) **(b)**

(c) **(d)**

Figure 3.3: Contact inspection

The inspection of the contacts (see fig. 3.3) showed a number of challenges:

- Bad adhesion of the contacts to the cross-linked PMMA
- platelets break the paths
- Proximity effect, especially at the centered platelet, see also appendix A.9

These challenges were the reason to develop a new contacting process which is described in chapter 2. Even though some of the issues were probably solvable, continuing with this approach was rated as too risky because of the unknown insulation properties of the thin cross-linked PMMA and the unpredictable time needed to solve the challenges mentioned above was estimated to take too long. The new idea, described in chapter 2 seemed to be a more promising approach and it turned out that covering the platelets with a resist layer, which is thick enough to serve as an insulation layer, was the answer to the challgenges.

3.2 Contacting

It turned out to be a big challenge to reach all the way to the top of the platelets with the contacts, see fig. 3.4.

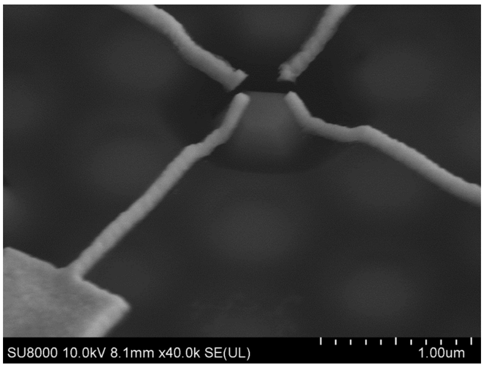

Figure 3.4: Contacts are not in touch with the platelets

The solution to this challenge was a combination of proper hole-ashing (see section 3.3), higher EBL exposure dose and improved aligning.

In order to make the alignment easier, the contact length and the hole-size were increased slightly for some write fields. The longer contacts made it easier to reach the platelets even if they are slightly misaligned.
The chance of uncovering the platelet increases with a bigger hole size aswell, even though if the hole pattern is not perfectly aligned above the target platelet.

The EBL exposure dose increased from $230\frac{\mu C}{cm^2}$ to $260\frac{\mu C}{cm^2}$ to $300\frac{\mu C}{cm^2}$ finally, which had together with the improved hole ashing the biggest impact on improving the contacting. The PMMA might be thicker in the etched hole since the liquid resist can't be flung away that easy in holes or trenches during the spinning process. The PMMA for the final contacting was probably not exposed the whole way down to the platelets surface therefore. That's why a thin PMMA layer probably remained on top of the platelets after the PMMA was developed. This thin layer probably prevented the contacts to reach the surface of the platelets. Exposing the PMMA all the way down to the platelets by increasing the dose made the resist soluble in the developer and the top of the platelets was uncovered totally.

3.3 Hole ashing

For a better understanding of the ashing behavior of the available EBL resists, dummy samples were used to investigate the etch rate of a PMMA 950 A8 and a ZEP 520 A7 resist for the used etch recipe (see section 3.3) on the RIE - Trion T2 etcher. The thickness was measured by an ellipsometer. It turned out that the etch rate for PMMA is with 12.6 Å/s slightly higher than the etch rate for ZEP, which is 9.8 Å/s, but they are similar, see fig. 3.6. Since the resist will be used for the hole-mask layer it needs to remain a certain time under the used ashing conditions before it disappears completely, see also section 2.7.1. The PMMA was chosen to be used because the achieved thickness of the resist layer was much bigger for the PMMA (≈ 600 nm) in comparison to the ZEP 520 A7 (≈ 300 nm) for a similar ashing behavior.

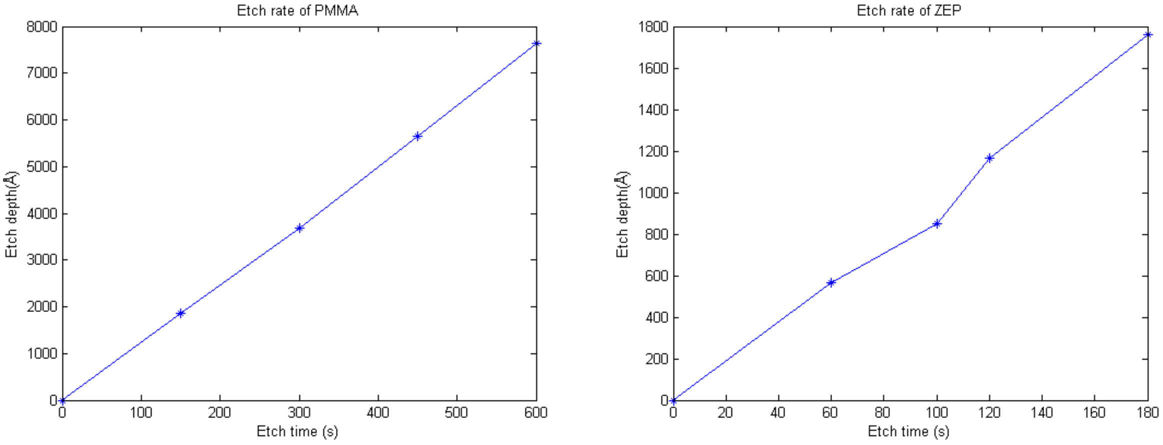

(a) **(b)**

Figure 3.5: Etch rates of PMMA and ZEP

Because the holes were located in a trench between the bond pads, it was investigated if different trench sizes have an influence on the etch depth caused by the RIE etcher. Four different sizes of strips were processed on dummy samples using the same process described in section 2.4.1. The trench sizes were 10μm, 20μm, 30μm and 50μm. The depth of the trenches were measured with a Profiler Dektak 6M before and after 600 seconds of the plasma ashing (see aslo section 3.3). The profiler measures the depth with the help of a diamond stylus which moves over the surface of a sample, the stylus experiences a displacement, when there is a change in surface profile. This displacement is equal to the change of the surface height.

No significant different etch depths were measurable for the investigated strip sizes after averaging the measured values for each strip size. It was decided to keep on processing with 10 μm strip size in order to insulate a bigger area of platelets with the lifting layer.

The etch process for uncovering the top of a platelet was interrupted by SEM sessions to check the etch status. It is easy to be fooled by a high acceleration voltage. One reason why the contacts of the early samples were not touching the platelets was because the hole was not etched deep enough. The higher the acceleration voltage, the deeper will the electrons be accelerated into the material and structures beyond the surface will become visible therefore. The holes looked perfectly fine with 10kV and the etch process was stopped. After further inspection with a lower acceleration voltage it turned out that the holes were probably not etched deep enough. In fig. 3.6 two SEM images of the same hole are shown, the acceleration voltage was 5kV for the first one, and 1kV for the second one. While the platelet is already visible in fig. 3.6a there is no sign of a structure beneath the surface in fig. 3.6b. Ever since the hole inspections were taken with a low acceleration voltage.

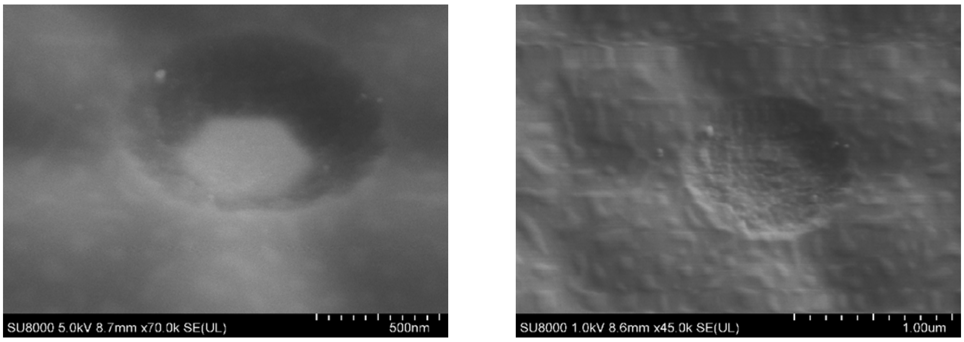

(a) Acceleration voltage: 5kV

(b) Acceleration voltage: 1kV

Figure 3.6: SEM inspection of the same hole

Further etch tests (see fig. 3.7) have shown that the etch rate for the hard baked Shipley resist is about three times lower than the etch rate for the PMMA. This might be due to the fact that the Shipley resist, the platelets are covered with is hard baked. Hard baked means that the polymers, the resist consists of are cross-linked and therefore less affected by the ions of the RIE etcher (see also appendix A.10). [18] While approximately 500 nm of PMMA were etched away, the resist was etched only 150 nm horizontally as well as vertically.

---

[18] Sami Franssila *„Introduction to Microfabrication - 2nd ed.“*; Wiley, Ltd, 106 (2010)

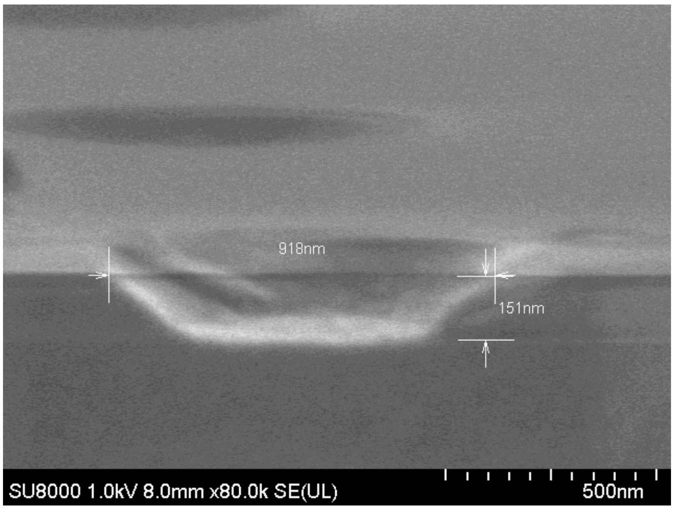

Figure 3.7: further hole inspection

4

Measurements

After the contact processing was done and a viable process to contact the GaN was developed, characterizing the electrical properties of the GaN structures was of interest. Therefore different kind of measurements were performed.

4.1 2-point measurments

The probe station Cascade 11000B was used for characterization, it contains four moveable arms, each arm is mounted with a needle to contact the probe. A screen connected to a microscope facing the sample helps to adjust the needles accurately to the bond pads on the sample. The probe is positioned on a metal board. To prevent that the sample slips out of space it got sucked to the board by a vacuum system. In order to isolate the sample from the metal board electrically, the probe was mounted to a plastic platelet before it was placed on the board. The probe station is controlled by a computer program, Keihley 4200 running on a computer that is connected to the needles.

The Probes were connected in the way, fig. 4.1 illustrates. A current was measured at the probes 1 and 2, while a voltage of ± 3V, swept in steps of 0,1V, was applied between the probes. The same was done for the probes 3 and 4.

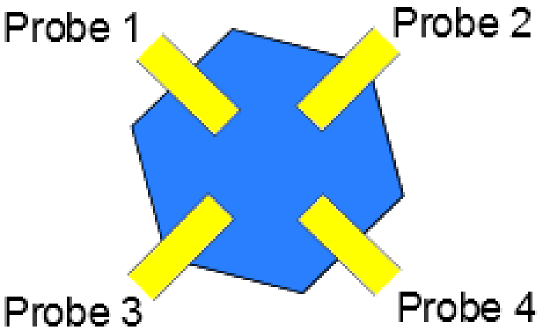

Figure 4.1: Top view and probe numbering

If the current had the identical value on both sides, the contacts are connected to the platelets since all other structures are electrically isolated this is the only possible current path. If there is no current measurable on the second probe, the contacts are not working. This first test was made for all 12 devices on each measured sample.

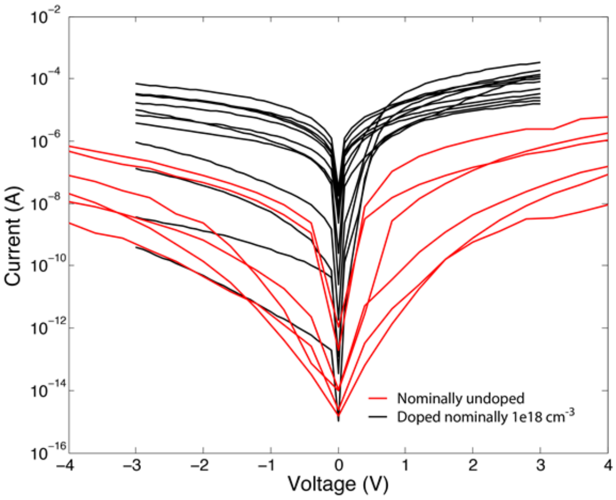

Figure 4.2: 2-point measurment

In fig. 4.2 the 2-point measurement results for the doped sample A in comparison to the undoped sample B are illustrated. The results are reasonable since the doped sample should have a smaller electrical resistance and therefore a higher electrical current than the undoped sample for the same voltage. Due to diversities in the contact qualities for different platelets it is necessary to take several measurements to get comparable data. Since the 2-point method doesn't count the contact resistance out another technique is required, which leads us to 4-point measurements.

4.2 4-point measurments

4-point measurements were performed on working write fields in order to achieve more accurate values for the resistance of the GaN platelet.

Every junction and every wire carrying current causes an electrical resistance. In our case we have a junction resistance where the contacts are touching the platelets and where the needles are sticking into the bond pads for instance. The goal is to avoid the impact these secondary resistances have on the measurements in order to get the value of the GaN resistance only. Therefore the voltage-sensing probes were separated from the pair of electrodes that were used to apply the current. In fig. 4.3 the comparison between the circuit model for the 2-probe to the one for the 4-probe measurement is shown. R_{cw} combines all contact and wiring resistances and R depicts the resistance of the platelet.

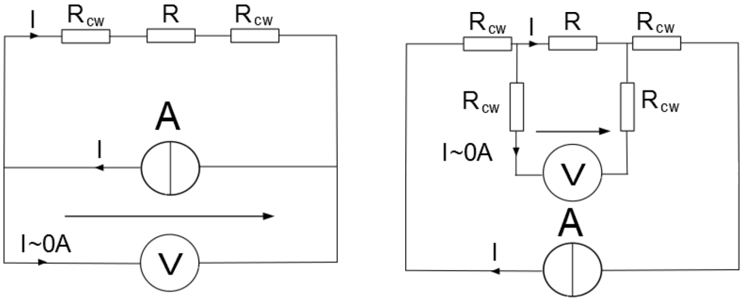

(a) 2-point circuit model **(b)** 4-point circuit model

Figure 4.3: Comparison between 2- and 4-point measurment

It is easy to see that the voltmeter senses the voltage drop on all resistances combined for the 2-point measurement. Secondary resistances won't disappear by using separate probes of course, but an ideal voltmeter has an infinite high input resistance, which means that the current is ideally zero in the voltmeter path hence the voltage drop at the resistances in this path is ideally zero as well. Therefore this unwanted influence is eliminated and the measurement yields to the GaN resist only. This specific 4-point measurement, which was performed in both ways fig. 4.4 illustrates is also called Van der Pauw measurement.

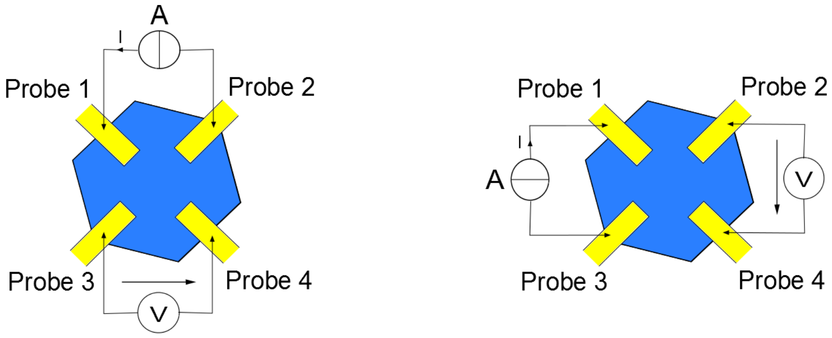

(a) **(b)**

Figure 4.4: 4-point measurment

The write fields, the 2-point measurement has shown that are working fine were used for further investigation with the 4-probe technique. First the current was applied by sweeping the voltage in fine steps. The same values as in the 2-point measurement were used to be on the safe side and not to destroy the structures. After safe current values were found, the procedure was performed again by sweeping the current in fine equidistant steps to achieve a proper voltage-current graph. In fig. 4.5 results of the measurement comparing the undoped sample B sample with the doped sample A are shown. The resistance for the undoped sample is about 3,8 MΩ and for the doped sample 2,7kΩ. The resistance of the undoped layer is about thousand times higher than the resistance of the doped layer. This indicates a low background doping for the undoped layer, which can be considered as an isolator to the doped layer therefore.

Getting data out of the undoped sample was difficult because of the small barely measurable currents.

The two resistances resulting out of the two measurments (see fig. 4.4) are in general not equal. Since the dimensions can be different for each measurment, the current paths don't have the same lengths necessarily and therefore in general two different resistances, R_1 and R_2.

$$e^{-\frac{\pi d}{\rho}R_1} + e^{-\frac{\pi d}{\rho}R_2} = 1$$

Where d is the thickness of the doped layer and ρ the electrical resistivity.

If there is at least one symmetrie axis in the structure and the contacts locations correspond to this symmetrie aswell, which is the case for our structures, the resistances are equal ($R_1 = R_2 = R$). Therefore we get a simplified approximation for the resistivity ρ:[19]

$$\rho = \frac{\pi d}{ln2} R \quad \sigma = \frac{1}{\rho}$$

With the electrical conductivity σ. For the sample A with a doped layer thickness of 46 nm and a resistance of 2.7 kΩ this results in:

$$\rho = \frac{\pi d}{ln2} R = 563 \cdot 10^{-6} \Omega m = 56.3 m\Omega cm \quad \sigma = \frac{1}{\rho} = 1.776 kSm^{-1} \tag{4.1}$$

These results seems to be reasonable, because similar values were discovered for Si-doped GaN with a compareable doping concentration before [20] [21].

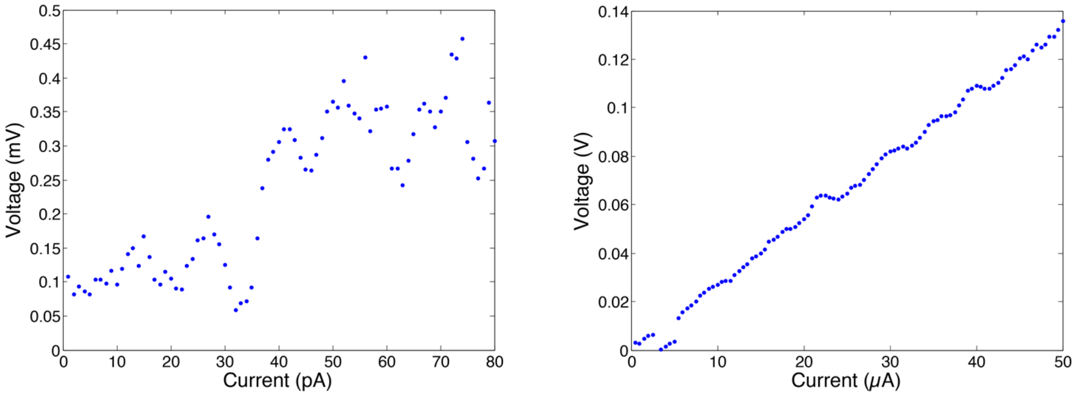

(a) undoped sample

(b) doped nominally 1e18cm^{-3}

Figure 4.5: 4-probe results

Hence the height of the volume, where charge carrier can move is limited to the height of the doped layer, because the isolating undoped layer is located underneath. Therefore significant **Hall measurements are possible**, because a defined height is prerequisite to get data out of Hall measurements.

---

[19] L. J. van der Pauw, „*A method of measuring specific resistivity and Hall effect of discs of arbitrary shape.* “; Philips Research Reports 13, 1, 1-9 (1958)

[20] P. Tcholfian, F. Donatini, F. Levy, P. Ferret et al.,„*High conductivity in Si-doped GaN wires* “; Appl. Phys. Lett., 102, 2013

[21] A. Wolos, Z. Wilamowski, M. Piersa and W. Strupinski, et al., „*Properties of metal-insulator transition and electron spin relaxation in GaN:Si*“; Physical Review B, 83, 165206 (2011)

4.3 Hall effect measurements

Some preparation was needed in order to amount the sample to the hall measurement setup. First it was cleaved to dimensions, so it can be glued on a IC (integrated circuit) socket. A bonding machine - K&S 4523 was used to connect wires from the bond pads to the socket. A careful handling of the sample was required to avoid electrostatic discharges that could destroy the devices therefore it was necessary to use a wristband connected to ground.

The Hall effect occurs in current-carrying conductors that are exposed to a stationary magnetic field and describes the appearance of a voltage perpendicular to both, the current direction and the magnetic field direction and is called Hall-voltage V_H, see also fig. 4.6a. The effect is based on the Lorentz-force F that distracts charge carriers which are moving with the velocity $\vec{v}$ and which are exposed to an magnetic field $\vec{B}$, perpendicular to their direction of movement.

$$Lorentz\ force: \vec{F} = q(\vec{E} + \vec{v} \times \vec{B})$$

Hence the charge carriers are forced to one side of the conductor or semiconductor, where a charge accumulation accrues and thus charge depletion will occur on the opposite side of the material. This charge distribution causes an electrical field strength $\vec{E}$ in the opposite direction to the Lorentz-force. This electrical field strength will stop the increasing charge separation caused by the Lorentz-force when both forces become equal.

$$Compensating\ electrical\ field\ strength: q(\vec{E} + \vec{v} \times \vec{B}) = 0$$

The separation of the charge carriers leads to the measureable Hall-voltage V_H. Assuming that the carriers move to the x-direction and the magnetic field is pointing to the z-direction leads to:

$$E_y - v_x B_z = 0$$

The current density in a conductor is $\vec{j} = nq\vec{v}$ where n is the electron concentration and q is the charge, which leads to $\vec{v} = \frac{\vec{j}}{nq}$, $\vec{v}$ inserted into the equation above leads to:

$$E_y = \frac{1}{nq} j_\times B_z = A_H j_\times B_z$$

$$E_y = \frac{U_H}{b}, j_x = \frac{I}{bd}$$

$$\rightarrow U_H = A_H \frac{IB_z}{d}$$

A_H is called Hall-constant, b is the width and d is the height.

The Hall-voltage can be used to calculate the charge carrier density out of the Hall-constant if the field and the thickness of the doped layer are given.

Together with the Van der Pauw results for the conductivity, the mobility of the particles can be calculated from the Drude conduction model, once the carrier density is known.

$$Drude\ conduction\ model : \sigma = q(n\mu_n + p\mu_p)$$

Where σ is the conductivity, p the hole concentration, μ_n the electron mobility and μ_p the hole mobility. Since sample A is n-doped, the Drude model simplifies to:

$$\sigma = qn\mu_n$$

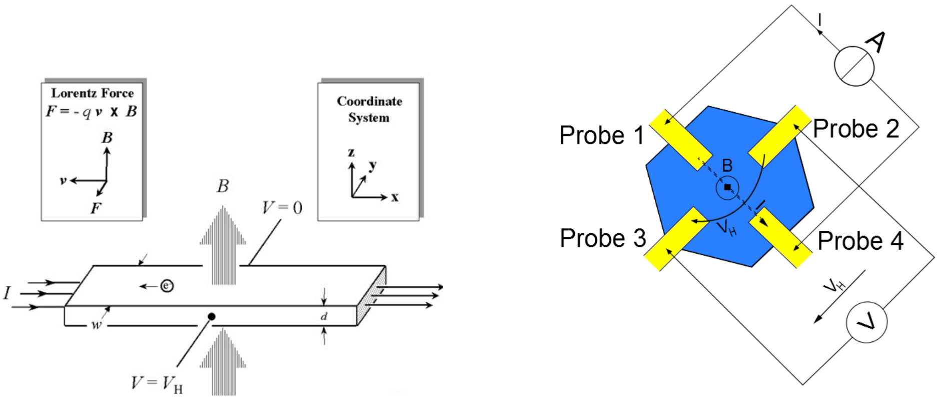

(a) Schematic of Hall effect [22]

(b) Top view of Hall measurment schematic

Figure 4.6

The samples were mounted onto a holder that was placed in the field of a electromagnet. A current was applied and the voltage was measured and displayed on a computer screen, see also fig. 4.6b.

As supposed the hall measurement was hard to perform for the undoped sample and

---

[22] *„http://www.nist.gov/pml/div683/hall_fig1.cfm “*

didn't lead to reasonable results due to the lack of moveable charge carrier.

A current of 1 μA was applied for the doped sample A. This current was chosen because it was highest possible current after the voltage compliance of the used electrometer was set to 3 V. This value was chosen to be on the safe side and not risking to destroy the device due to a high electrical field since the 2-point measurement has been already performed up to the same voltage level (see also fig. 4.1).

During increasing or decreasing the magnetic field, the measured voltage responded by changing significantly. After the magnetic field was stationary again, the voltage level was slightly different to the value it had before the field was changed. In fig. 4.7a a measurement of sample A at the write field 18 is visibl. The violet voltage values in fig. 4.7a correspond to a field change from 188.5 mT to 0.06 mT. The difference between the voltage before and after the field change is the Hall-voltage. The measurement was very sensitive to changes in the environment, like the light switch. Therefore the sample was shielded with an aluminum casing and the used cables were twisted to increase the electromagnetic compatibility. Many voltage values to the same magnetic field were measured and averaged to get a more significant result. This resulted in fig. 4.7b, the measurement started at a magnetic field of 0.06 mT first it was increased to 102.5 mT before it was changed to 185.5 mT and finally decreased again to 0.06 mT, to see if the curve ends up at a value close to the initial point again. The exact value of the field was measured by a gaussmeter.

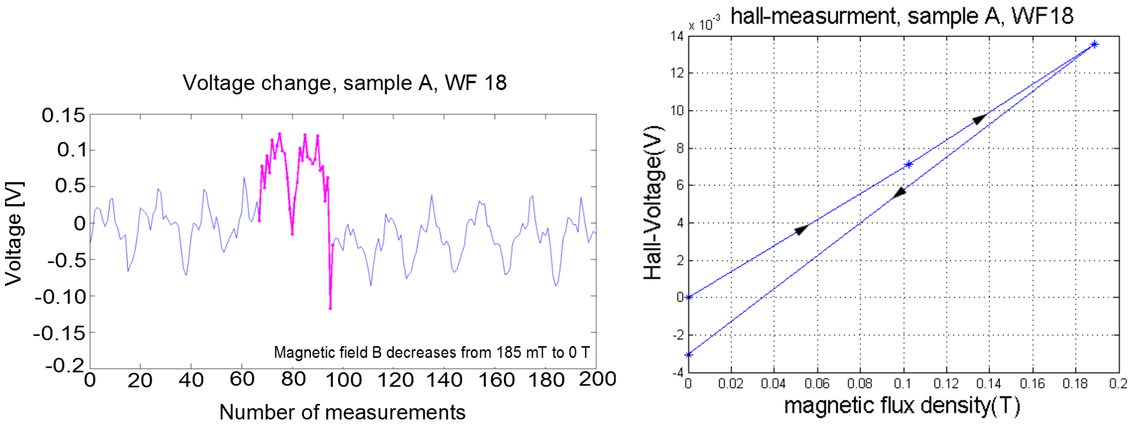

(a) **(b)**

Figure 4.7

The formula for the Hall voltage can be used to calculate the carrier density:

$$U_H = \frac{IB_z}{dnq} \rightarrow n = \frac{IB_z}{U_H dq}$$

Taking the values for the second measured point (see fig. 4.7) into account delivers:
$U_H = 13.8\ mV$
$B_z = 188.5\ mT$
$I = 1\ \mu A$
$d = 46\ nm\ (see section\ 1.5)$
$q = 1.6 \cdot 10^{-19}\ As$

$$n = \frac{IB_z}{U_H dq} \approx 1{,}86 \cdot 10^{21} \frac{1}{m^3} = 1{,}86 \cdot 10^{15} \frac{1}{cm^3} \tag{4.2}$$

Which is obviously different from the actual doping level of $10^{18} \frac{1}{cm^3}$. One have to take into account that the contacts are big in comparison to the sample size and that they extend quite far into the sample.

Ideal contacts would be infinitesimal small and would be located at the periphery of the sample[23]. The location and the dimensions of the contacts are not taking into account in eq. (4.2) but the contact size and -symetry as well as the length, the contacts are extending into the sample influence the hall measurements[24].
Furthermore, it's difficult to meassure very small voltage drops (μVs are expected, see fig. 5.4) with the available measurement set up, since the expected Hall signal would be units smaller than the variations in the voltage measurements, (see fig. 4.7a) which are not caused by the Hall effect. Plans to improve the set up exist. The electromagnetic compatibility needs to be improved, the used cables should be shorter, the floor would need to be grounded ideally and the power supply should be decoupled from the main power supply for instance.

But eventhough the values are incorrect, the measured voltages responded always immediately with the correct sign to a change of the magnetic field, which **indicates the**

---

[23] *„Lake Shore 7500/9500 Series Hall System Users Manual, APPENDIX A: HALL EFFECT MEASUREMENTS“*; http://www.physics.oregonstate.edu/ tate/TateLabWiki/lib/exe/fetch.php?media=hall:manual_app_a_hallmeasurementsystem.pdf

[24] S. Sanfilippo, *„HALL PROBES: PHYSICS AND APPLICATION TO MAGNETOMETRY“*; Paul Scherrer Institut, Villigen, Switzerland, 2011

Hall effect.

Together with the conductivity from the Van der Pauw measurment (eq. (4.1)), the carrier mobility would be:

$$\sigma = qn\mu_n \rightarrow \mu_n = \frac{\sigma}{qn} \approx 5.97\frac{m^2}{Vs} = 5.97 \cdot 10^4 \frac{cm^2}{Vs}$$

Which is not meaningful, due to the incorrect value of the doping level from the Hall-measurement. Other research groups found a carrier mobility of $240\frac{cm^2}{Vs}$ [25] for Si doped GaN, which is about 250 times smaller.

Performing these measurements on nanoscale structures is one of the main challenges in this work. In contrast to macroscopic samples, the contact dimensions cannot be neglected anymore. The contacts are big in comparison to the nanoscale dimensions of the sample and affect the Hall effect measurement. In order to improve the measurements, a goal should be to decrease the contact size aswell as the length they extend into the sample and increase the distance between the probes. Furthermore, the symetry of the contacts should fit to the symetry axis of the sample.

---

[25] In-Hwan Lee et al., „*Mobility enhancement and yellow luminescence in Si-doped GaN grown by metalorganic chemical vapor deposition technique* “; Journal of Crystal Growth 182, 314-320, 1997

5

Simulation

A platelet of the 1e18 doped sample A was chosen to be simulated in COMSOL in order to compare the behaviour of the simulated Hall with the actual measured values. The simulations allow to make an assessment whether the experimental data, gained from the measurements having the correct value and behavior for different doping profiles. It can be modified easily to different samples with different dimensions of the platelet or the contacts. Therefore a 3D model was built with the identical dimensions as the platelets have on the sample. A current-continuity model was created.

Because of the presence of a magnetic field the Ohm's law is:

$$\overline{J} = -\overline{\sigma}\nabla V \overline{J} = -\overline{\sigma}\overline{E} \tag{5.1}$$

Wehre $\overline{J}$ is the current density tensor, V the electrical potential and sigma the conductivity tensor under the influence of the magnetic field. Because of the presence of the magnetic field the charged particles will move into the direction of the electrical field but also into the direction of the Lorentz-force. Therefore a conductivity tensor is necessary that includes the influence of the magnetic field on the particle trajectory. With the assumption that $\overline{B} = (0,0,B)$ is pointing into the z-direction, the conductivity tensor becomes[26]:

$$\overline{\sigma} = \sigma_0 \begin{pmatrix} \frac{1}{1+(\omega\tau)^2} & -\frac{\omega\tau}{1+(\omega\tau)^2} & 0 \\ \frac{\omega\tau}{1+(\omega\tau)^2} & \frac{1}{1+(\omega\tau)^2} & 0 \\ 0 & 0 & 1 \end{pmatrix} \tag{5.2}$$

Where $\sigma_0 = \frac{q^2 n\tau}{m}$ is the isotropic conductivity and the cyclotron radius $\omega = \frac{qB}{m}$ with the particle mass m, the electrical charge q, the scattering time τ and the charge carrier density n.

The conductivity tensor is derivated as followed[26]:

$$Lorentz\ force : \vec{F} = q(\vec{E} + \vec{v} \times \vec{B}) \tag{5.3}$$

Taking the motion of charge carriers in conductive materials into consideration, the eq. (5.3) can be written as:

$$m\frac{d\vec{v}}{dt} + \frac{\vec{v}}{\tau} = q\vec{E} + q\vec{v} \times \vec{B} \tag{5.4}$$

Where t is the time, m the particle mass and τ the scattering time. Since we assumed tat $\vec{B}$ points into the z-direction, the eq. (5.4) can be splitted up into:

$$m\frac{dv_x}{dt} + \frac{v_x}{\tau} = q(E_x + v_y B)$$

$$m\frac{dv_y}{dt} + \frac{v_y}{\tau} = q(E_y + v_x B)$$

$$m\frac{dv_z}{dt} + \frac{v_z}{\tau} = qE_z$$

Steady-state: $\frac{dv_x}{dt} = \frac{dv_y}{dt} = \frac{dv_z}{dt} = 0\frac{m}{s^2} \rightarrow$

$$v_x = \frac{\frac{q\tau}{m}(E_x + \omega\tau E_y)}{1 + (\omega\tau)^2}$$

$$v_y = \frac{\frac{q\tau}{m}(E_y + \omega\tau E_x)}{1 + (\omega\tau)^2}$$

$$v_z = \frac{q\tau}{m}E_z$$

After the introduction of ω and a comparison with eq. (5.1), the elements of the conductivity tensor $\overline{\sigma}$ can be found which results in eq. (5.2) with the isotropic conductivity

$\sigma_0 = \frac{q^2 nt}{m}$.

The original model (fig. 5.1a) took too much computing for performing a mesh (fig. 5.1c) and therefore it needed to be simplified slithtly (fig. 5.1b). Unfortunately, the simplified contacts differ to the used contacts. In order to safe time, only the top regions of the platelet were simulated with a high resolution because this region is the area of interest.

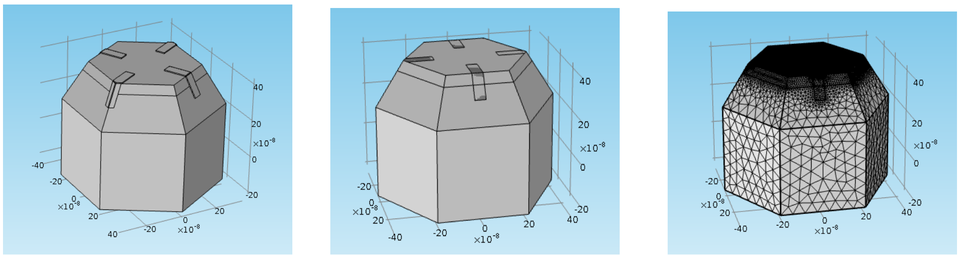

(a) original model **(b)** simplified model **(c)** meshed model

Figure 5.1

A current of 1 μA, which was used for the measurements was applied between two contacts in the simulation. The simulated electrical potential in a cross-sectional plane for the applied current is illustrated in fig. 5.2. The color-bar next to the model describes the relation between the potential and the color. The highest potential can be found in the red area at the contact where the current was applied. The lowest potential, indicated by blue color can be found at the contact on the opposit side of the plane where ground was defined.

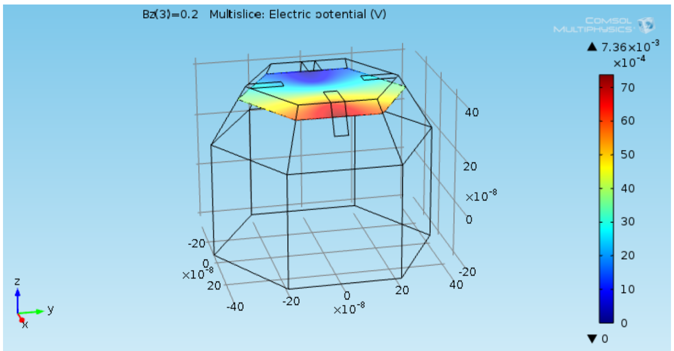

Figure 5.2

The magnetic field $\vec{B}$ points into the z-direction and its simulated values are 0 T 0.1

---

[26] Kristian Storm, „*Novel Processing and Electrical Characterization of Nanowires* “; Lund University, Division of Solid State Physics, 19, 2013

T and 0.2 T. In fig. 5.3 a cross-sectional plane illustrating the electrical potential between the Hall voltage sensing probes, perpendicular to the current direction is shown.
Since the interesting area in the simulation is the top region of the platelets and the other areas were meshed with a low resolution.
Since the plane is perpendicular to the current and there is no magnetic field applied, the electrical potential is the same at the at the upper left and upper right of the plane, see fig. 5.3a.
When $\vec{B}$ increases to 0.1 T (fig. 5.3b) and 0.2 T (fig. 5.3d) the Hall-effect becomes visible. Charge carriers will be deflected and accumulate on one side and deplet at the opposit side of the platelet. This effect can be seen by the color-change in the illustrations in fig. 5.3. A accumulation of charge carriers causes an increase of the electrical potential and a depletion of charge carriers causes a decrease of the electrical potential. A voltage can be measured because of the different potential levels. The difference between the voltage level before and after a change of the magnetic field is the Hall voltage.

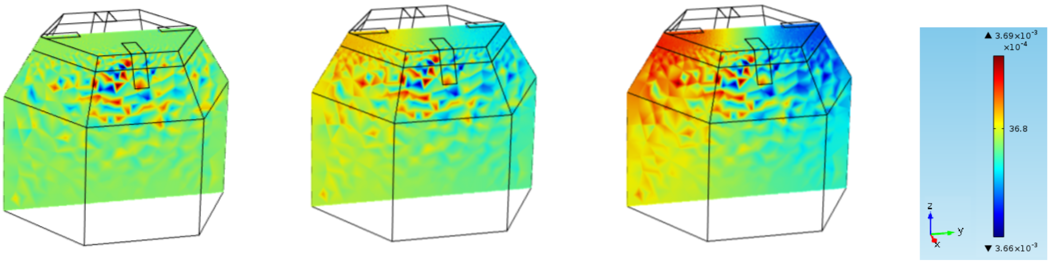

(a) B = 0 T **(b)** B = 0.1 T **(c)** B = 0.2 T **(d)**

Figure 5.3: Hall-signal

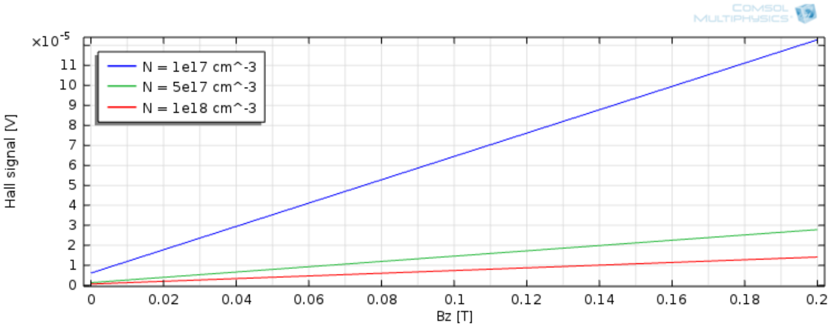

Figure 5.4: Hall voltage for different doping levels

The graph in fig. 5.4 shows the results of the Hall-simulation for various doping concentration. The background doping was assumed to be $10^{15}\ \frac{1}{cm^3}$.

The measured value for the Hall voltage is with $\approx 1 \cdot 10^{-5}$ V not close to the simulated value, which is no big suprise since the measured value turned out to be incorrect and the contacts of the simplified model have a slightly different shape in comparison to the used contacts.

Another reason why the Hall measurment didn't work properly could be found in the size of the expected value for the Hall voltage. The simulation has shown that values about 10 μV are expected for the Hall signal. A look at fig. 4.7a shows that such a voltage drop is probably not measureable with the available Hall-setup since the variations in the measured voltage, that are not originating in the Hall effect are units bigger than the expected Hall signal.

Since the background doping of the "undoped" area is not known, the influence of different background dopings (N_b) was simulated in fig. 5.5. It was assumed that the top layer has a doping level of $10^{18}\ \frac{1}{cm^3}$, the same as for sample A.

The higher the resistivity beneath the doped layer, the more significant are the results of the Hall measurement, because these measurements depends on a well defined thickness of the investigating layer. The difference between the influence on the Hall signal for a background doping of $N_b = 10^{15}\ \frac{1}{cm^3}$ and $N_b = 10^{16}\ \frac{1}{cm^3}$ is minimal.

As fig. 5.5 shows, the measurments become inaccurate if the background doping increases further to $N_b = 10^{17}\ \frac{1}{cm^3}$. This means that the resistivity of the the undoped layer decreases, hence more charge carriers moving from the doped layer on the top of the platelet into the undoped layer beneath. The electrical potential caused by these charge carriers won't be measured correctly by the contacts since they are located on the top of the platelet.

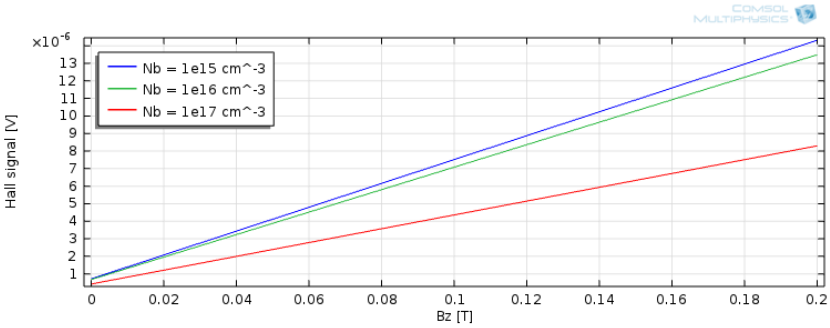

Figure 5.5: Hall voltage for different background doping

The results of this simulation can be helpfull for future Hall measurements, to compare the results for different doping profiles as well as to investigate the influence of different dimensions of the platelet and the contacts, as well as the contact location, since the model can be modified easily.

6

Conclusion

Electrical characterization of nanostructures are usually limited by the inability to determine fundamental properties, such as doping level and carrier mobility. Since this information is crucial for the development of electrical devices based on these structures, it is necessary to find a way to contact these nanoscale materials and investigate their properties. Hall- and 4-probe measurements are a way to measure the doping level and the carrier mobility.

A viable contacting process for 4-point and 2-point measurements of sub micro-sized planarized platelets was achieved successfully. This was confirmed by performing 2- and 4-probe measurements which lead to reasonable results.

These results indicates that Hall-measurements on the GaN pyramid-structures are possible.

Hall-measurments were tried but the measured values were inaccurate. However, the supposed Hall voltage responded for all measurements with the correct sign to a change of the magnetic field, indicating the Hall effect.

Now that a viable process is developed, more samples with different doping levels and different contact dimensions need to be investigated with Van der Pauw and Hall-measurements and get compared, in order to provide more significant data.

Development of Schottky contacts and Ohmic contacts to evaluate the break down voltage could be the next step before HEMT's can finally be developed.

A

Used processes and techniques[27]

A.1 MOVPE

Metal organic vapor phase epitaxy (MOVPE), see fig. A.1 is a complex process to grow single crystalline thin films by chemical reaction of metal organics at elevated temperatures on the surface of a substrate. The metal organics evaporates at room temperature and are stored in so called bubblers. With help of carrier gases, like hydrogen or nitrogen the organic compounds are transported to a reaction chamber, where the deposition on the substrate takes place. The reaction chamber is pumped down to coarse vacuum.
MOVPE became the most important manufacturing method for III/V semiconductors. Two metal organic compounds are trimethylgallium $(CH_3)_3Ga$ and ammoniacNH_3 for instance, which can be used to grow GaN, a chemical equation can be seen in eq. (A.1).

$$(CH_3)_3Ga + NH_3 \rightarrow GaN_{(solid)} + 3CH_{3(gas)} \tag{A.1}$$

The GaN remains on the surface while the by-products will be removed.

---

[27] Gary S. May, Simon M. Sze*„Fundamentals of Semiconductor Fabrication“*;Wiley Inc; 2003

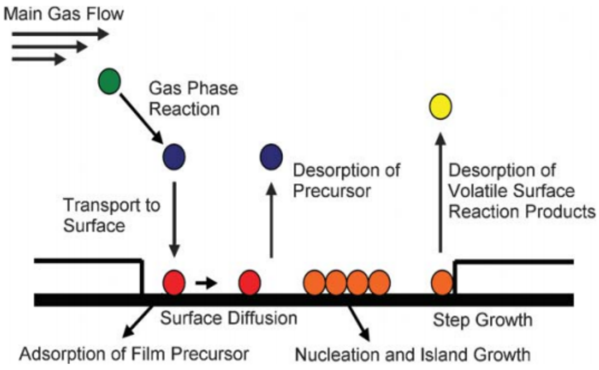

Figure A.1: Principle of MOVPE-process [28]

A.2 Annealing

Annealing is basically used in order to heal out crystalline structures, like semiconductors. By heating up the material to a certain temperature for a certain time, impurities can be removed, furthermore crystal constellations can rearrange and thus getting rid of lattice dislocations. In order to prevent the materials from new impurities the structures will be heated up in a vacuum chamber where dissolved impurities will be pumped out.

A.3 ALD

Atomic Layer Deposition, see also fig. A.2 is a process which allows a precise thickness control of the deposited thin film and works at relatively low temperatures (about 150 °C), but has only a weak throughput.

The process can be repeated several cycles. One atomic mono layer will be deposited ideally per cycle. A characteristic property of the ALD is the use of self-limiting chemical reactions including at least two precursors.

The first step in a cycle is to vent a chamber, which is heated up and pumped down to low pressure with the first reactant (precursor). This gas is reacting only with the surface of the solid material but not with itself and is therefore self-limiting, thus a single layer of the reactant is deposited.

---

[28] Jamie S. Ritch, Tristram Chivers, Mohammad Afzaalb and Paul O'Brien, *„The single molecular precursor approach to metal telluride thin films: imino-bis(diisopropylphosphine tellurides) as examples* “; Chemical Society Review, 36, 1622-1631 2007

The second step is to evacuate the reaction chamber with a non-reactive inert gas in order to remove everything that didn't react with the surface of the target material.
The third step is to vent the chamber with another precursor gas to activate the deposited layer for the reaction in the first step again therefore it's possible to deposit a new layer.
The fourth and last step of a cycle is to purge the reaction chamber with an inert gas again, for the same reason as in the second step.

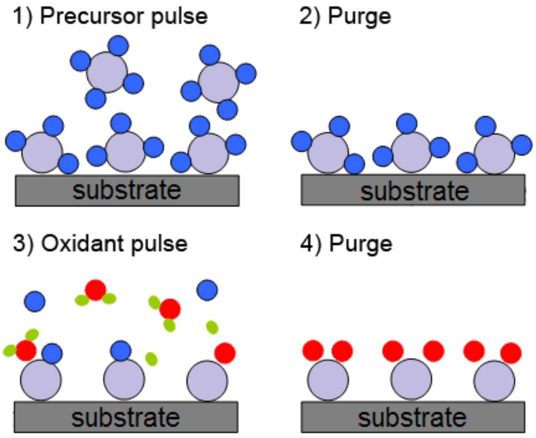

Figure A.2: Principle of an ALD-cycle [29]

A.4 Ellipsometer

An Ellipsometer transmits linear or circular polarized light in a certain angle to the surface of the sample and measuring the change in the polarization, which is dependent among others to the thickness of the surface layer. Hence the thickness can be deduced out of the polarization change, see fig. A.3.

---

[29] *„http://npl-web.stanford.edu/archive/energy/micro-fuel-cell/sofc/electrode/ald/ “*

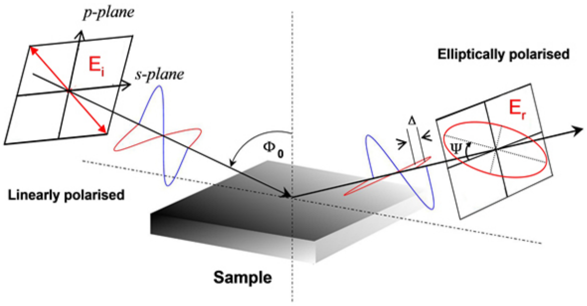

Figure A.3: Principle of an Ellipsometer [30]

A.5 Spin-coating

As the name suggests, a spinner is rotating with an adjustable orbital speed for an adjustable time. The probe is fixed to the spinner by getting sucked to a planar attachment of choice due to a vacuum pump. The resist will be placed on top of the sample and by adjusting the orbital speed and time the desired resist thickness can be reached. The spinner spreads the resist uniformly over the top of the surface.

A.6 Photolitography

The pattern of a photo mask will be projected to a photoresist by illuminating the mask with the resist beneath. The light changes the chemical properties of the resist after it get exposed by light. Therefore a proper alignment of the mask to the probe is very important. There are two different types of photo resists, the exposed areas are getting soluble in the developer solution if it's a positive resist and insoluble if it's a negative one.

A.7 Plasma Ashing

Plasma ashing is a dry etching-process is caused by a chemical surface reaction thus it is highly isotropic and material selective, since different elements reacts different with the same reactant. A plasma asher contains a reaction chamber, which is pumped down to a low pressure (e.g. 5mbar) before the chamber will be flooded up to a few milli-bars

---

[30] *„http://www.tcd.ie/Physics/Surfaces/images/elli_dia.JPG "*

with the etch gas (e.g. Oxygen). A high frequent electromagnetic field forms a reactive plasma out of the etch gas which attacks the surface of the probe. The absorbed reaction products will be pumped away by the vacuum system. The time the electromagnetic field is created is adjustable and determines the etch time and is therefore proportional to the etch rate.

A.8 Evaporator

An Evaporator is used to deposit a metal of choice unto the surface of a target. The samples are amounted upside down at the top of a chamber, so that the target surface is facing downwards. The preferred metals are inserted into heat resistant boats which are located at the bottom region of the chamber. Afterwards the chamber will be pumped down to a very low pressure (e.g. 10e-8 bar) before the boat that contains the chosen metal will be heated up until the metal in it melts and evaporates to the top of the chamber where it deposits on the surface of the target samples. Because of the vacuum conditions in the chamber the evaporated particles won't scatter on any other matter in the chamber hence the trajectory of the evaporated metal is straight to the top and thus the process is highly anisotropic. The thickness of the deposited layer is well-controlled by a shield which protects the sample, by moving it underneath it from further evaporated particles if the aimed thickness is reached.

A.9 EBL

Electron beam lithography uses the same principle as optical photolithography but as the name suggests an electron beam is used instead of electromagnetic waves and therefore a different kind of resist is necessary, which is sensitive to the electrons. The dose of electrons is adjustable and instead of a physical mask a computer program is used to control the EBL-equipment where the mask can be uploaded and created with a CAD-program. The chemical properties of the resist change when it gets hit by the electrons and becomes soluble to the development solution. The exposed areas will be washed away while the others will remain on the substrate.

The big advantage to optical lithography is that there is no need for a mask and the much smaller structures (some nano meters) that can be created. While the optical lithography is limited by its wavelength, the wavelength of electrons with a typical energy used for EBL is some pico-meters. The resolution depends on the beam diameter and is affected by phenomena like forward- and backscattered electrons, the creation of

secondary electrons and the proximity effect. The electrons can be scattered by hitting other particles in the resist, these scattered electrons can expose unintentionally an area of the resist. By transmitting the impulse of the particles, a secondary electron can created which can expose a wider area of the resist and due to electrical interactions neighbor electrons can be influenced and expose adjacent areas as well, which is known as the proximity effect.
A disadvantage is that the process times are economically unsatisfactory for mass production.

A.10 Reactive Ion Etching

In difference to plasma ashing (see also, appendix A.7) the process is not purely chemically. And in difference to ion milling, which is a pure physically etch process where the surface will be atomized due to the momentum transfer of the impacting ions, also called sputtering, the RIE process is using reactive ions. It's a mix between the two mentioned processes. The plasma is created by an electrical field and the chemical reaction on the surface is initialized by the kinetic energy of the impacting ions. Therefore the electric field is accelerating the ions towards the sample holder. The desorbed etching-products will be pumped up by a vacuum system. The setup is similar to the already explained plasma ashing (see also, appendix A.7) with a reaction chamber, which has a gas inlet and is pumped down to a low pressure. The gas flow, pressure, field power and the etch time are adjustable and controlled by a computer connected to the equipment. Due to its chemical and physical properties the etch process includes an isotropic as well as an anisotropic component.

Bibliography

1: S.J. Pearton, F. Ren, A.P. Zhang, K.P. Lee, *„Fabrication and performance of GaN electronic devices“*; Materials Science and Engineering, Reports: A Review Journal, 55 (2000)

2: „Silicon Carbide and Gallium Nitride Power Semiconductors - World - 2013“; IMS Research marked analysis, (2013)

3: Zhaoxia Bi, *„Dislocations“* ;unpublished image by courtesy of Zhaoxia Bi.

4: L. Liu, J. Edgar, *„Substrates for gallium nitride epitaxy“*; Materials Science and Engineering R 37, 61-127 (2002)

5: B. Beamount, Ph. Vennegues, P. Gibart, *„Epitaxial Lateral Overgrowth of GaN“*; physica status solidi (b), 227 (2001)

6: Pierre Gibart, *„Metal organic vapour phase epitaxy of GaN and lateral overgrowth“*; Reports on Progress in Physics, 667 (2004)

7: Patent: WO 2013121289 A2, QuNano AB, *„Gallium nitride nanowire based electronics“*; 12.2.2013

8: Kihyun Choi, MunetakaArita, YasuhikoArakawa, *„Selective-area growth of thin GaN nanowires by MOCVD“*; Journal of Crystal Growth 357 ,58–61 (2012)

9: Stephen D. Hersee, Xinyu Sun, Xin Wang, *„The Controlled Growth of GaN Nanowires“*; Nano Letters Vol. 6, No. 8, 1808-1811 (2006)

10: Stephen D. Hersee, Ashwin K. Rishinaramangalam, Michael N. Fairchild, *„Threading defect elimination in GaN nanowires“*; Cambridge Journals Material Research, Vol. 26, No. 17; 2293 (2011)

11: Zhaoxia Bi, *„GaN buffer with dislocations. Dislocations don't grow up into a nanowire“* ;unpublished image by courtesy of Zhaoxia Bi.

12: J. H. Ryou et al., *„Control of quantum-confined Stark effect in InGaN-based quantum wells“*; IEEE of Selected Topics in Quantum Electronics, 15, 1080 (2009).

13: S. Strite and H. Morkoc, *„GaN, AIN, and InN: A review“*; American vacuum society, 1237 (1992).

14: J. C. Zolper, R. G. Wilson, S. J. Pearton, and R. A. Stall, *„Ca and O ion implantation doping of GaN“*; Applied Physics Letters, 68, 1945 (1996).

15: *„s1800 series Data Sheet“*; http://nanofab.ece.cmu.edu/resources/s1800seriesDataSheet.pdf.

16: *„PMMA Data Sheet“*;http://microchem.com/pdf/PMMA_Data_Sheet.pdf

17: M. A. Mohammad, M. Muhammad, S. k. Dew, M. Stepanova *„Fundamentals of Electron Beam Exposure and Development “*; Springer, 2012.

18: Sami Franssila *to Microfabrication - 2nd ed.“*; Wiley, Ltd, 106 (2010)

19: L. J. van der Pauw, *„A method of measuring specific resistivity and Hall effect of discs of arbitrary shape.“*; Philips Research Reports 13, 1, 1-9 (1958).

20: P. Tcholfian, F. Donatini, F. Levy, P. Ferret et al.,*„High conductivity in Si-doped GaN wires“*; Appl. Phys. Lett., 102, 2013.

21: A. Wolos, Z. Wilamowski, M. Piersa and W. Strupinski, et al., „*Properties of metal-insulator transition and electron spin relaxation in GaN:Si*“; Physical Review B, 83, 165206 (2011).

22: „*Schematic of Hall effect*“;http://www.nist.gov/pml/div683/hall_fig1.cfm

23: „*APPENDIX A: HALL EFFECT MEASUREMENTS*“; Lake Shore 7500/9500 Series Hall System Users Manual, Lake Shore Cryotronics, Inc., Westerville, OH.

24: S. Sanfilippo, „*HALL PROBES: PHYSICS AND APPLICATION TO MAGNETOMETRY*“; Paul Scherrer Institut, Villigen, Switzerland, 2011.

25: ln-Hwan Lee et al., „*Mobility enhancement and yellow luminescence in Si-doped GaN grown by metalorganic chemical vapor deposition technique* “; Journal of Crystal Growth 182, 314-320, 1997.

26: Kristian Storm, „*Novel Processing and Electrical Characterization of Nanowires* “; Lund University, Division of Solid State Physics, 19, 2013.

27:Gary S. May, Simon M. Sze„*Fundamentals of Semiconductor Fabrication*“; Wiley Inc, 2003

28: Jamie S. Ritch, Tristram Chivers, Mohammad Afzaalb and Paul O'Brien, „*The single molecular precursor approach to metal telluride thin films: imino-bis(diisopropylphosphine tellurides) as examples* “; Chemical Society Review, 36, 1622-1631 2007.

29: „*Principle of an ALD-cycle* “;http://npl-web.stanford.edu/archive/energy/micro-fuel-cell/sofc/electrode/ald/

30: „*Principle of an Ellipsometer*“; http://www.tcd.ie/Physics/Surfaces/images/elli_dia.JPG